Local structural changes in polyamorphous (Ni,Fe)O_x electrocatalysts suggest a dual-site oxygen evolution reaction mechanism

Martin A.W. Schoen,[†] Nicholas M. Randell,[†] Oliver Calderon,[†] Santiago Jimenez Villegas,[†] Katelyn M. Daly,[†] Roman Chernikov,[‡] and Simon Trudel*[,†]

†*Department of Chemistry and Institute for Quantum Science and Technology, University of Calgary, 2500 University Dr NW, Calgary, AB T2N 1N4 Canada*

‡*BIOXAS Beamline, Canadian Light Source, 44 Innovation Boulevard, Saskatoon, SK, S7N 2V3, Canada*

E-mail: trudels@ucalgary.ca

Abstract

Amorphous nickel-iron mixed metal oxides have been shown to be extremely efficient oxygen evolution reaction (OER) electrocatalysts with good stability in alkaline reaction conditions. Thus, they offer an economical alternative to expensive conventional platinum- or iridium-based OER catalysts and could provide a crucial step towards a hydrogen-based energy economy. These favorable properties are presumably due to a synergistic effect between Fe and Ni. However, these synergistic effects strongly depend on the local structure of the catalyst and their origin – and its relation to the local structure – are still not fully understood. In this work we present a study of the thermal annealing induced structural evolution of amorphous (Ni,Fe)O_x thin films, and correlate this evolution to their OER catalytic capabilities. Samples are x-ray amorphous at low annealing temperatures. However,

analysis of the x-ray absorption spectra reveals local structural transitions in all samples – before the onset of cystalization – providing evidence of polyamorphism. Transitions of the local Ni and Fe environments occur at distinctly different temperatures and coincide with a stepwise increase in the catalytic activation potential (OER thermodynamics) and the Tafel slope (OER kinetics), respectively. We previously have attributed the increase in onset potential to a change in active site in NiO_x at the phase transition temperature; considering that the mixed metal oxides' onset potentials exhibit the same behavior with annealing temperature (T_{anneal}), we conclude that the potential-determining OER reaction step must occur at a Ni site. Similarly, the reaction kinetics change at the same annealing temperature as the local Fe environment; we thus infer that the rate-determining step occurs at a Fe site. To reconciliate these observations we put forward a dual-site OER reaction mechanism with potential- and rate-determining steps happening at Ni and Fe sites, respectively. This synergistic effect is ultimately responsible for the superior OER performance of many (Ni,Fe)O_x catalysts. At higher annealing temperatures, the synergistic effect is suppressed, possibly by phase separation into NiO_x and FeO_x phases, as suggested by our XRD results.

Keywords

oxygen evolution reaction, amorphous materials, synergistic effects, x-ray absorption fine structure, dual-site mechanism, electrocatalysis

Introduction

In the fight against rising greenhouse gas emissions, hydrogen-based fuels and energy storage could play a significant role in the development of a decarbonized energy landscape.[1] However, the current storage system cycle efficiency for an electrolyzer/fuel cell solution lies below 40 %; higher efficiencies need to be achieved to make hydrogen fuels competitive on the market.[2] Widespread implementation of the hydrogen economy hinges on a concomitant development

and adoption of cost-efficient renewable energy schemes such as solar, tidal, and wind, while also increasing the efficiency of water electrolysis without incurring prohibitive costs. The hurdle to the latter goal is the facile handling of the kinetically sluggish four-electron oxygen evolution reaction (OER).[3] One class of materials that has received significant interest over the past years are mixed metal oxides of nickel and iron ((Ni,Fe)O_x), as they show remarkable catalytic activity for the oxygen evolution reaction, are sourced from Earth-abundant metals, and are (for the most part) stable under reaction conditions.[4,5]

(Ni,Fe)O_x catalyst occur in a variety of configurations. NiFe layered double hydroxides (LDHs) have been shown to be highly efficient for OER applications. With overpotentials at 10 mA cm^{-2} of less than 200 mV LDHs are amongst the most efficient OER catalysts; however they can suffer from long-term stability issues. A comprehensive summary of NiFe LDH catalyst properties can be found in Ref. 6. (Ni,Fe)O_x nanoparticles provide large surface areas, can exhibit targeted structures and surface orientations or non-equilibrium compositions, as well as beneficial substrate interactions They are thus a versatile group of (Ni,Fe)O_x catalysts.[7–10] However, efficient size/shape control and substrate adhesion can be detrimental to their OER performance.[6] Amorphous (Ni,Fe)O_x is easily fabricated and thus amongst the most cost-efficient NiFe-based catalysts; it exhibits high OER efficiency[11,12] similar to LDHs and is stable under OER conditions.[11] However a lack of detailed understanding of the local amorphous structure and different polyamorphs prohibits targeted engineering of the catalytic properties. These groups of (Ni,Fe)O_x catalysts cannot be strictly separated and the list is by no means exhaustive.

However, the exact OER mechanism and nature of the catalytically active site[5] in all these (Ni,Fe)O_x material systems is still disputed, as evidenced by many different, often contradictory reports.[13–23] Nevertheless, the large diversity of internally consistent reports on the properties of (Ni,Fe)O_x catalyst and underlying reaction mechanisms illustrate a key point: catalytic properties are predominantly determined by local structure rather than catalyst composition. This has been confirmed in studies where Fe was incorporated in a Ni host material *via* different

methods, each resulting in distinctly different catalytic properties.[16,24] However, such studies are merely snapshots of structure and performance. Investigating a continuous structural evolution in catalysts made via the same method could provide a better picture of the catalytic reaction. This idea inspired us to investigate the structural evolution of amorphous mixed metal Ni-Fe oxides and their catalytic properties, as an extension of our previous work on nickel oxides.[25] Such studies are especially important for amorphous materials, which are challenging to characterize structurally, making structure-property relationships difficult to delineate.

In this study, we use photochemical deposition to produce (Ni,Fe)O_x thin films with well-defined Fe:Ni ratios. This method yields highly amorphous metal oxides,[11,25–28] and has the ability to make mixed-metal oxides with easily controlled stoichiometry.[29–31] From the as-prepared amorphous state, structural change is induced by annealing the films in air at various temperatures. We electrochemically benchmark these (Ni,Fe)O_x films by determining the Tafel slope, and measuring overpotential at catalytic onset at 10 mA cm^{-2}. The Ni-Fe mixed metal oxide system shows the now well-documented synergistic OER catalysis[11,12,32] with catalytic performance significantly exceeding the pure metal oxides.

Structural properties are monitored by K-edge x-ray absorption spectroscopy (XAS) and x-ray diffraction (XRD). We find all compositions undergo an amorphous-to-amorphous phase transition as they are annealed. Surprisingly, these local environment transitions occur at different temperatures for each metal site. The XRD detection limit is reached at higher annealing temperatures than the phase transition for each sample series, confirming the amorphous nature of these phase transitions and the existence of distinct polyamorphs in the (Ni,Fe)O_x material system.

Our main finding is that the dependence on annealing temperature of the potential determining step (PDS) correlates with structural transitions at the Ni site, while the kinetics of the reaction correlate with structural transitions at the Fe site. This seemingly contradictory behavior can be explained by a dual-site OER mechanism, where one or more OER intermediate steps occur at a given metal site and then transfer to the other metal site for the remaining reaction

steps. This unique investigation into the structural evolution of polyamorphous (Ni,Fe)O_x OER electrocatalysts provides unprecedented experimental insight into local environment, catalytic activity, and how Ni and Fe sites synergistically facilitate the OER.

Experimental

Amorphous (Ni,Fe)O_x thin films were prepared using photochemical deposition as previously reported.[11,12,33] Film compositions range from FeO_x to NiO_x in 25 atomic-% increments, which will be henceforth referred to as **Fe_{100}**, **$Fe_{75}Ni_{25}$**, **$Fe_{50}Ni_{50}$**, **$Fe_{25}Ni_{75}$**, and **Ni_{100}**. The recently investigated series of annealed **Ni_{100}** is included for completeness and comparison.[25] These films were used as-prepared (*i.e.* **Ni-AP**) or annealed in air at various temperatures (*i.e.* **$Fe_{75}Ni_{25}$-XXX**, where "**XXX**" is the annealing temperature T_{anneal}). Sample preparation and full experimental details are provided in the Supporting Information.

Results and Discussion

XRD

The XRD patterns of selected (Ni,Fe)O_x thin films are plotted in Fig. 1a. XRD patterns without discernible peaks were omitted. No other diffraction peaks attributed to the (Ni,Fe)O_x films were found in the measured range of 15° to 70°. The **Fe_{100}** series only exhibits α-Fe_2O_3 (104) diffraction peaks for $T_{\text{anneal}} \geq 600$ °C, which get narrower with increasing T_{anneal}. All the mixed metal oxides annealed at 800 °C and higher exhibit the α-Fe_2O_3 (104) diffraction peak to different degrees, however at T_{anneal} = 800 °C the **$Fe_{75}Ni_{25}$** and **$Fe_{50}Ni_{50}$** samples additionally show a α-Fe_2O_3(110) peak. The **$Fe_{25}Ni_{75}$** series exhibits both α-Fe_2O_3 (104) and NiO (111) peaks, indicative of phase separation at high T_{anneal}. **Ni_{100}** samples crystallize at the lowest T_{anneal}, with the NiO (111) diffraction peak already detected for **Ni_{100}-400**. This peak gets incrementally narrower with increasing T_{anneal}. The NiO (200) diffraction peak only appears for **Ni_{100}-1000**. We

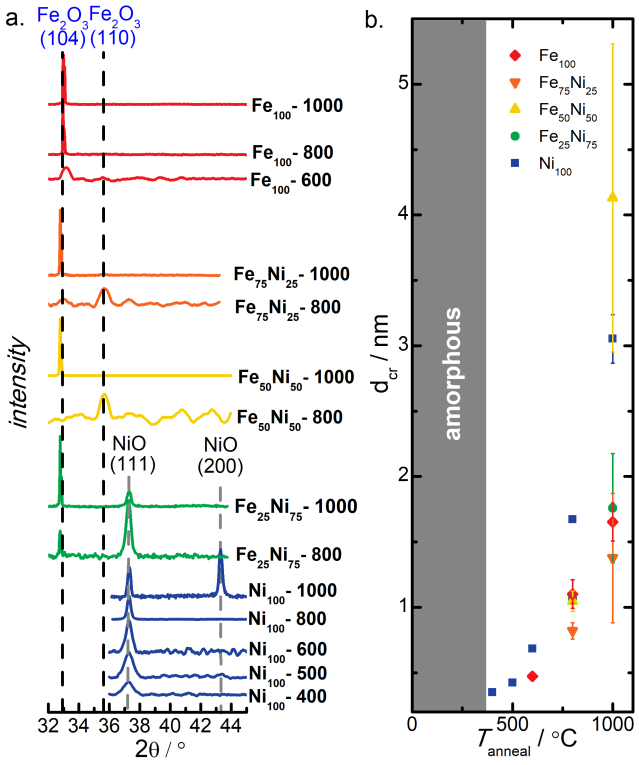

Figure 1: a. XRD patterns of (Ni,Fe)O_x samples. Only patterns for samples exhibiting diffraction peaks are plotted. The position of α-Fe_2O_3(104) and (110), as well as NiO(111) and (200) Bragg peaks are denoted with dashed lines. b. Crystallite sizes d_{cr} determined from Eq.S1 are plotted against T_{anneal}.

calculate the crystallite size d_{cr} from Eq. S1 and plot it in Fig. 1b. As expected, we observe an increase in crystallite size with T_{anneal}, which is more pronounced in Ni-rich samples. With the exception of one data point the incorporation of Fe seems to inhibit the crystallite growth and the mixed metal oxides and the pure FeO_x exhibit smaller d_{cr} than the pure NiO_x samples.

X-ray absorption spectroscopy

X-ray absorption spectra were collected for the annealed sample series, as well as on selected electrochemically treated *post-operando*, henceforth labelled as **PO** samples. Electrochemical treatment conditions are detailed in the SI.

XANES

XANES spectra at the Fe and Ni K edges, along with spectra of α-Fe_2O_3, FeOOH, NiO, and $Ni(OH)_2$ reference compounds are plotted in Fig. 2. The **Fe_{100}** Fe K edge XANES qualitatively resembles FeOOH for low T_{anneal} and evolves towards α-Fe_2O_3 as T_{anneal} increases; this shift occurs at a T_{anneal} between 300 and 400 °C. Similarly, the **Ni_{100}** XANES spectra closely resemble $Ni(OH)_2$ below T_{anneal} = 250 °C and evolves to NiO for higher T_{anneal}. These qualitative observations are supported by linear combination fitting of FeOOH and α-Fe_2O_3 or $Ni(OH)_2$ and NiO for the Fe or Ni edge respectively(Figs. S6 and 5).

The mixed (Ni,Fe)O_x samples qualitatively exhibit similar trends for the Fe (Ni) edge, showing a transition from a FeOOH-like ($Ni(OH)_2$-like) to a α-Fe_2O_3-like (NiO-like) lineshape. These transitions occur at different T_{anneal} for the Fe and Ni centers. At the Fe edge the transition approximately occurs at 500 °C for the mixed metal oxides, while the Ni edge XANES shows a transition at lower T_{anneal} of 400 °C for all sample compositions. These transitions are however more gradual and the transition temperatures less well-defined than in either of the pure metal oxides. For all (Ni,Fe)O_x samples, linear combination fitting with only two standards fails to fully reproduce the data (especially at high T_{anneal}) and including additional reference spectra does not improve the fit, indicating some degree of component intermixing. However linear combination fitting does allow us to determine the onset of the coordination transition in the mixed metal alloys, as shown in Fig. 5.

Post-operando samples were also investigated by XAS. The **Ni_{100}-AP-PO** sample shows a small (~ 1 eV) edge position shift towards higher energies when compared to the untreated samples, with no significant change in lineshape. This energy shift decreases linearly to zero by **Ni_{100}-400-PO**. All Fe edge **PO** XANES spectra shift to lower energies (~ -1.2 eV) and qualitatively resemble the Fe_3O_4 standard, however linear combinations of Fe_3O_4 and α-Fe_2O_3 did not yield satisfactory fitting. Both energy shifts at the Ni and Fe edge are close to the achievable energy resolution (≈ 0.7 eV), since we cannot take simultaneous reference foil spectra in fluorescence mode. Similarly, the pre-edge feature of the **PO** samples shifts to lower energies, consistent with

a transition to Fe_3O_4,[34] however this shift of approximately 0.2 eV is significantly smaller than our energy resolution (0.7 eV) and we are not able to make a definite statement.

The XANES edge position is commonly used to determine the average oxidation states.[34] We utilize the method described by Smith *et al.*[27] to determine the oxidation state of our samples, which is based on comparing the energy spacing between edge and pre-edge positions to the value of reference compounds. The determined oxidation states are presented in Fig. S7. All Fe edge oxidation states scatter within errors around +3, as expected for a α-Fe_2O_3- or FeOOH-like environment, while Ni edge oxidation states scatter within errors around +2, as expected for a $Ni(OH)_2$- or NiO-like environment. In the **PO** series all Fe edge oxidation states scatter around a value of +2.6, indicative of a Fe_3O_4 like structure, while the Ni edges of the mixed metal oxides exhibit oxidation states of approximately +2. Only the oxidation state of the **Ni_{100}-PO** series shows a dependence on T_{anneal} by decreasing steadily from +2.5 for **Ni_{100}-AP-PO** to +2 by **Ni_{100}-400-PO**.

EXAFS

The Fourier transform of the EXAFS spectra is plotted in Fig. S3 for all samples. Modeling of the Ni and Fe K edge EXAFS (methodology is described in the SI) yields the coordination number N, first shell M-O bond distances, second shell M-M bond distances, and Debye-Waller factors, which are plotted against T_{anneal} in Figs. 3 and S4. All fit parameters are reported in Tables S1-S4.

The Fe coordination number N scatter within errors around a value of 6 with no discernible trend with T_{anneal} or composition. A N of 6 is usually associated with a fully coordinated octahedral environment, as is expected for both α-Fe_2O_3 and FeOOH.[34] The **PO** series N (see Fig. S5) exhibit a similar independence with T_{anneal}, albeit with generally lower values than the annealed series.

N for the Ni edge exhibits lower values of approximately 4.5 for all **AP** samples, as we previously reported for **Ni_{100}**.[25] This value increases with T_{anneal} for all samples; step wise at T_{anneal} = 250 °C for the **Ni_{100}** samples, and more continuously for the bimetallic series. N of the **PO** se-

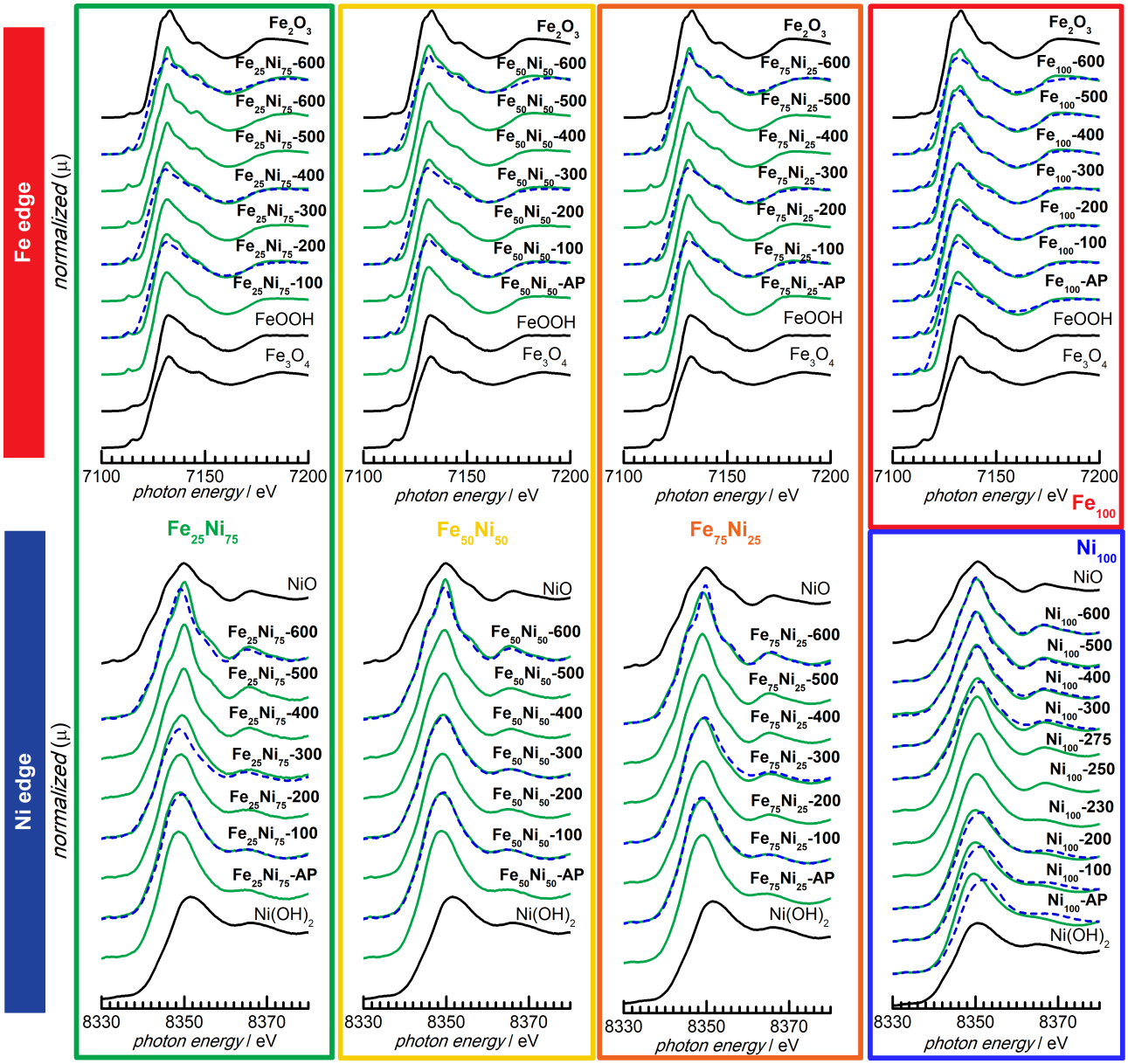

Figure 2: Fe (upper row) and Ni (lower row) K edge XANES spectra for (Ni,Fe)O_x samples annealed at various temperatures. Spectra for untreated annealed samples are plotted as solid green lines, **PO** samples as blue dashed lines, and FeOOH, $Ni(OH)_2$, α-Fe_2O_3, Fe_3O_4, and NiO reference compounds as black lines.

ries mimics this behavior, however with marginally lower values (Fig. S5). This indicates that the Ni atoms are on average under-coordinated at low T_{anneal} and only reach full octahedral coordination with annealing.

The first- and second- shell bond distances are shown Fig. 3. The Fe-O bond distances for all samples scatter around the α-Fe_2O_3 $R_{\text{Fe-O}}$ (1.96 Å[35]) with no discernible trend with T_{anneal} or composition. At the Ni edge, samples **Ni_{100}-AP** through **Ni_{100}-200** exhibit a Ni-O bond distance of 2.05 Å, characteristic of $Ni(OH)_2$.[35] This bond distance then increases stepwise to the NiO-characteristic[35] bond length of 2.075 Å by **Ni_{100}-300**. In the mixed metal oxides the Ni-O bond distances seem to exhibit lower $Ni(OH)_2$-like bond distances at low T_{anneal} and increase gradually with higher annealing temperatures. However, this trend is ambiguous when considering the associated error bars, and thus does not give a clear indication of a coordination transition similar to the one occurring in **Ni_{100}**.

The behavior of the second shell M-M bond distances with T_{anneal} and sample composition is more complex. The Fe-Fe distance in the **Fe_{100}** series decreases step-wise from approximately 3.13 Å in **Fe_{100}-AP** to the α-Fe_2O_3 value of 2.98 Å at **Fe_{100}-400**. In the **$Fe_{75}Ni_{25}$** series the Fe-M and the Ni-M bonds decrease from 3.17 Å and 3.08 Å for the **AP** sample to 3.05 Å and 2.95 Å by sample **$Fe_{75}Ni_{25}$-400** and **$Fe_{75}Ni_{25}$-600** respectively. A similar, almost linear decrease for both metal-metal distances is observed in the **$Fe_{50}Ni_{50}$** series. On the Ni-rich side in the **$Fe_{25}Ni_{75}$** series, the Fe-M bond distance only marginally decreases from 3.1 Å to 3.075 Å over the measured range of T_{anneal}, while the Ni-M bond decreases from 3.05 Å for **$Fe_{25}Ni_{7}$5-AP** to 2.98 Å for **$Fe_{25}Ni_{75}$-400** and stays constant for higher T_{anneal}. The Ni-Ni bond distance is approximately 3.08 Å for **Ni_{100}-AP** and decreases to the characteristic NiO distance by **Ni_{100}-300**.

We observe that the Ni and Fe coordination environments are strongly influenced by the mixing. The stepwise changes occurring in the pure metal oxides are smoothed out and the shift in coordination environments is drawn out to higher T_{anneal}. The intermixing of Fe and Ni stabilized the low-temperature amorphous phase. Specifically this means that Ni-M bond distances gradually converge to the NiO crystalline reference distance with increasing T_{anneal},

while Fe-M distances are converging to a distance of approximately 3.075 Å, which is significantly larger than the α-Fe_2O_3 value.

With the exception of the NiO_x samples, the **PO** samples follow the same trends with no significant deviation. In the **Ni_{100}** series the Ni-oxygen bond distance increases from 1.97 Å for the **AP** sample to 2.075 Å for **Ni_{100}-500-PO**, see Fig. S5.

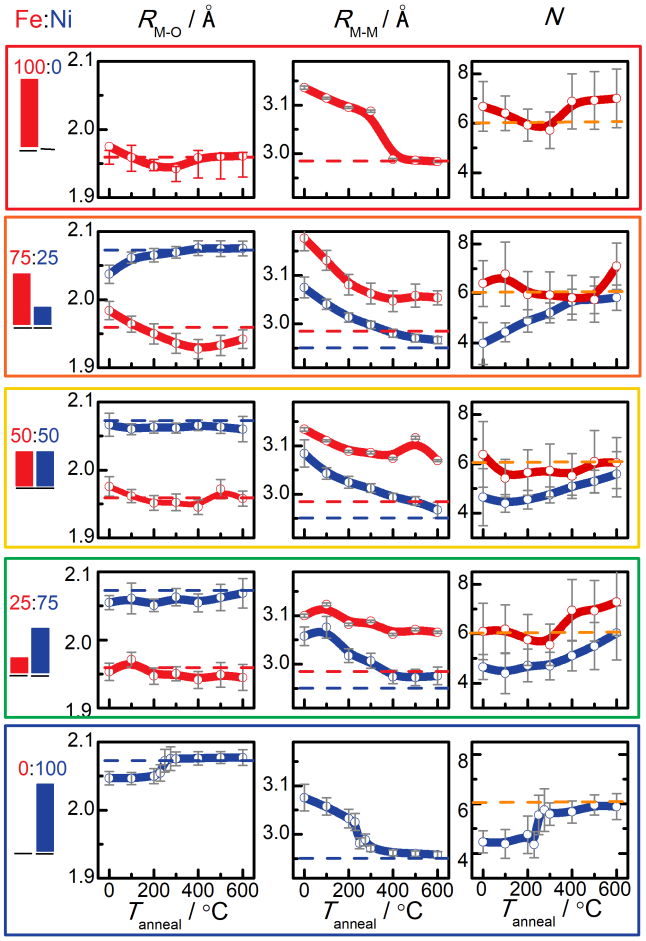

Figure 3: Metal-oxygen bond distances (R_{M-O}, left column), metal-metal bond distances (R_{M-M}, middle column), and coordination number N (right column) are plotted against T_{anneal} for the sample composition denoted on the LHS. Fe edge data are plotted in red, Ni edge data in blue. Lines are guides to the eye. Crystalline NiO and α-Fe_2O_3 reference bond distances are plotted as dashed lines in the respective colors in the LHS and middle panel columns and the octahedral coordination $N = 6$ is plotted as an orange dashed line in the RHS panel column.

Electrochemistry

Measured cyclic and step voltammetry can be found in the SI in Fig. S8. Overpotentials (η) at catalytic onset and at 10 mA cm^{-2} are plotted in Fig. 4 a. In the **Fe$_{100}$** series η at onset stays approximately constant with T_{anneal} around a value of 0.25 V. With increasing Ni content the onset overpotential of the **AP** samples drops dramatically to 0.14 V for **Fe$_{75}$Fe$_{25}$-AP** and decreases further with Ni content to 0.1 V for **Ni$_{100}$-AP**.

η at onset increases with T_{anneal} in all Ni containing samples – continuously for samples in the **Fe$_{75}$Fe$_{25}$** series and more step-like for the series with higher Ni content. This step-wise increase starts at T_{anneal} = 225 °C for **Ni$_{100}$** and at approximately 300 °C for **Fe$_{25}$Fe$_{75}$** and **Fe$_{50}$Fe$_{50}$** and thus coincides with the observed structural transition in EXAFS, compare Fig. 3. By T_{anneal} = 600 °C η at onset has increased by approximately 0.1 V in all Ni containing samples. It is worth emphasizing the similarities of the T_{anneal} dependence of the onset potentials in the mixed metal oxides to the pure NiO_x series and the stark difference of this behavior in the pure FeO_x series. The overpotential η at 10 mA cm^{-2} follows the trends described for the onset overpotentials with an offset of approximately 0.3 V for all Fe-containing samples and approximately 0.4 V in the **Ni$_{100}$**. These overpotentials are in the range of reported values of comparable materials.[6,11,12]

Measured Tafel slopes are plotted in Fig. 4 b. The Tafel slope in the **Ni$_{100}$** series decreases almost linearly from 100 mV dec^{-1} for the **Ni$_{100}$-AP** to 60 mV dec^{-1} for **Ni$_{100}$-600**. In the **Fe$_{100}$** series the Tafel slope first decreases from a value of approximately 70 mV dec^{-1} for **Fe$_{100}$-AP** to 55 mV dec^{-1} by **Fe$_{100}$-300** to then increase back to 70 mV dec^{-1} for **Fe$_{100}$-600**. As previously reported,[11,12,32] Tafel slopes for the mixed metal oxides are significantly lower than for pure Ni or Fe oxides. For low T_{anneal} all mixed metal oxides exhibit low Tafel slopes (within errors below 40 mV dec^{-1}), with the lowest value of 34 ± 5 mV dec^{-1} achieved for **Fe$_{25}$Ni$_{75}$-200**. The Tafel slopes of the (Ni,Fe)$O_x$series increase with T_{anneal} above 400 °C and reach values close to 60 mV dec^{-1}. So while at low T_{anneal} the reaction kinetics of the mixed metal oxides are significantly improved compared to NiO_x or FeO_x, they slow down with annealing concurrent

with the Fe phase transition and Tafel slopes become comparable to the pure oxide Tafel slopes.

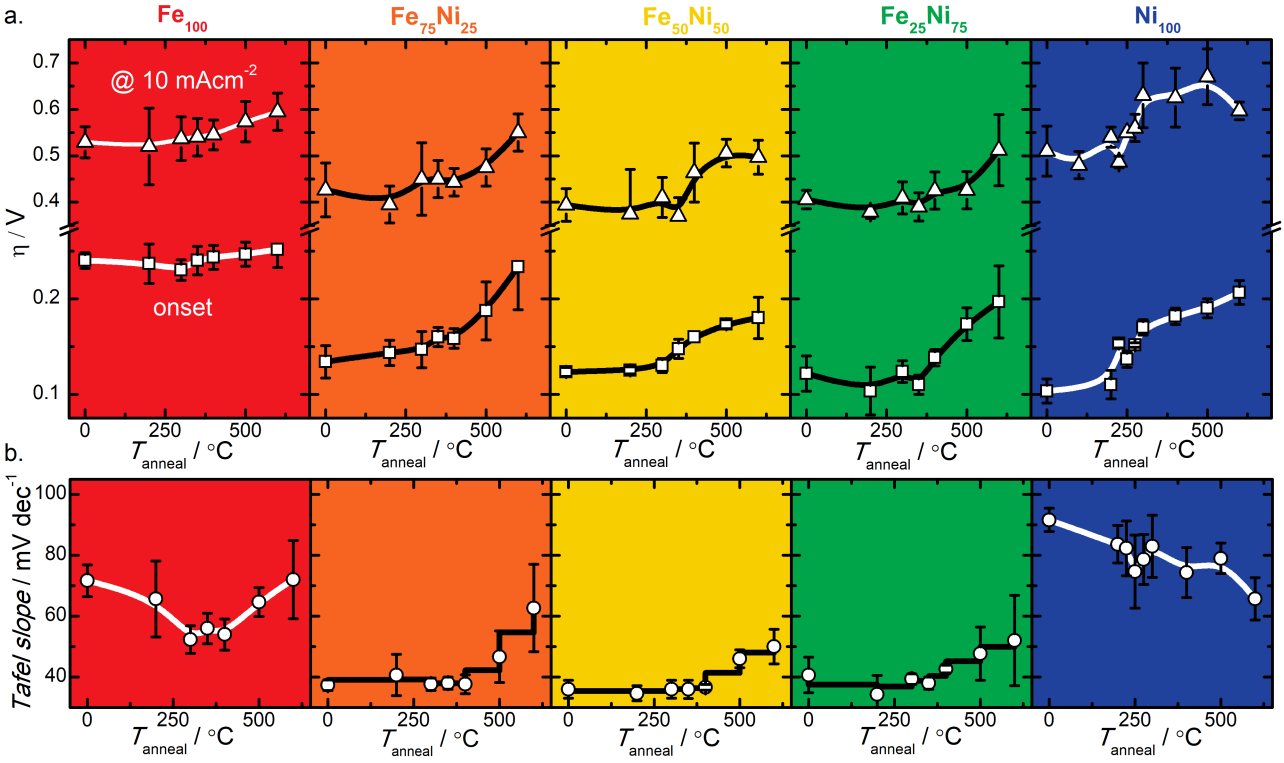

Figure 4: a. Overpotentials η at catalytic onset (squares) and at 10 mA cm^{-2} (triangles) are plotted vs. T_{anneal} for all denoted sample compositions. b. Tafel slopes are plotted against T_{anneal} for the denoted sample compositions. Everywhere, lines are again guides to the eye.

Discussion

Structure

Structurally, we find transitions of the coordination environment in all materials. XANES linear combination fitting of the Fe edge (Fig. 5) shows a transition from a FeOOH-like environment to a α-Fe_2O_3-like environment at T_{anneal} = 400 °C in the **Fe$_{100}$** series. This same transition occurs around 500 °C in the mixed metal oxides. For Ni, a transition from a $Ni(OH)_2$-like to a NiO-like environment occurs at lower annealing temperatures of 300 °C for **Ni$_{100}$**, and 400 °C for the mixed metal oxides. These transitions can also qualitatively be observed in the EXAFS spectra (Fig. S3). For Ni the second coordination shell peaks (at a reduced R of approximately

2.5 Å) increase in amplitude at the phase transition temperatures. Similarly, for the Fe a second peak characteristic of α-Fe_2O_3 appears at approximately 3 Å at the respective phase transition temperature. These phase transitions occur before XRD diffraction peaks are detected, thus demonstrating the existence of amorphous polymorphs (polyamorphs) in all sample series. A remarkable effect of the incorporation of Fe into NiO_x or vice versa is that the mixing impedes both crystalline growth and stabilizes the low-temperature amorphous phase. This stabilization of the amorphous phase possibly provides an explanation for the exceptional stability of amorphous (Ni,Fe)O_x catalysts under reaction conditions.

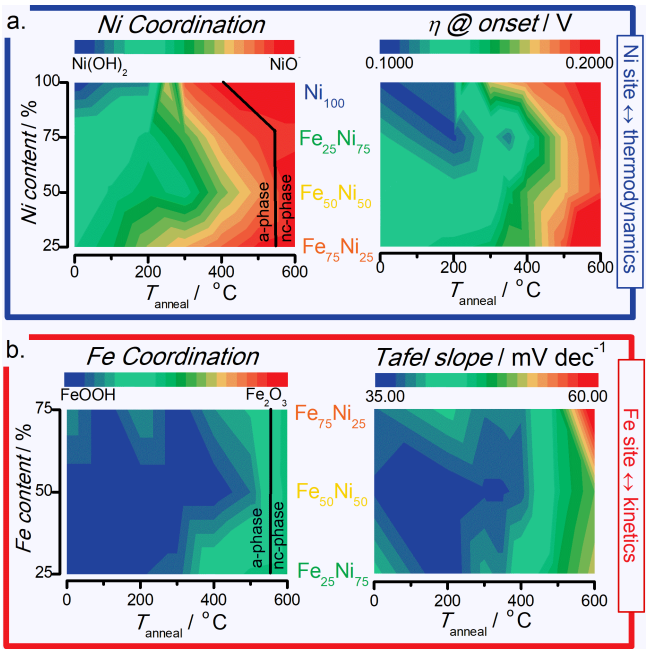

Figure 5: **a.** Ni coordination environment from XANES linear combination fitting (left) and onset overpotentials (right) are plotted as a function of Ni content and T_{anneal} to illustrate the correlation between Ni edge coordination transition and increase in onset potential (reaction activation potential, or thermodynamics). **b.** Correlation between Fe edge coordination transition and Tafel slope (reaction kinetics) for the mixed metal oxides. Interpolation via contour plots is reasonable, since the observed quantities change little with sample composition. The black lines in **a.** and **b.** indicate the approximate transition temperatures between amorphous (a-phase) and nano-crystalline (nc-phase) phases.

An analysis of the EXAFS parameters, shown in Fig. 3, confirms the existence of a coordination transition in both systems. However, this transition proceeds rather differently in the pure metal oxides than in the mixed metal oxides. In $\mathbf{Ni_{100}}$ the Ni-O and Ni-Ni distances and N

change stepwise at the transition temperature. For **Fe$_{100}$**, this stepwise change is only apparent for the second coordination shell ($R_{\mathrm{Fe-Fe}}$). This transition is still present – albeit more gradual – in the mixed metal oxides, as evidenced by the gradual shift in these same EXAFS parameters. It is worth noting that the Fe local environment is exclusively octahedral with approximately constant Fe-O bond lengths for all compositions and annealing temperatures. In contrast, the Ni environment changes from an under-coordinated octahedral (or possibly tetrahedral) coordination at low T_{anneal} to fully coordinated octahedral at high T_{anneal}, accompanied by an extension of the Ni-O bonds for all samples.

As we will explain, the Fe-M and Ni-M bond exhibit distinctly different values, indicating a distinctly different coordination environment between Fe and Ni, yet these coordination environments are influenced by the other metal species. Bond angles in the mixed metal oxides cannot be exactly determined, given the identity of the nearest next-neighbor metal atom cannot be unambiguously determined and Fe and Ni exhibit distinctly different M-O bond distances. However, in the pure metal oxides the Fe-O-M bond angles can be evaluated from the Fe-M bond distances, where 90 ° indicates edge-sharing octahedra, and higher angles corner-sharing octahedra. In the **Fe$_{100}$** series neighboring FeO_6 octahedra transition from being predominantly corner-sharing – with Fe-O-M bond angles centered around 105° ($R \sim 3.12$ Å) – to a mixture of corner- and edge-sharing octahedra, as evidenced by an average Fe-O-M bond angle of 99° ($R \sim 2.99$ Å). These bond angles are in the range of previously reported values[26] and the existence of a combined corner and edge sharing octahedra phase has been shown in pair distribution function measurements on the FeO_xsystem.[28] The addition of Ni does not significantly alter the first-shell octahedral coordination, but affects the FeO_6 octahedra packing, by marginally promoting the larger Fe-O-M angle edge-sharing configuration. The packing trends to either smaller Fe-O-M bond angles, or to an increased fraction of edge-sharing octahedra with increasing T_{anneal}. The Ni second shell coordination at low T_{anneal} cannot be described in a similar fashion as we do not know the exact nature of the first shell coordination (under-coordinated octahedral vs. tetrahedral). For higher T_{anneal} however, the Ni first coordination

shell is fully octahedrally coordinated, and the second shell bond distances indicate an almost exclusively edge sharing environment (Ni-O-M bond angle ≈ 91°), as expected for the NiO structure. As previously stated, the addition of Fe stabilizes the low T_{anneal} $Ni(OH)_2$-like phase with larger Ni-M bond distances to higher T_{anneal}. However, when annealed at 600 °C all samples converge to the predominantly edge sharing NiO-like octahedra configuration.

A similar influence of compound mixing on structural properties has been observed in amorphous thin film oxides,[36] however in NiFe layered double hydroxides no difference between Ni edge and Fe edge bond lengths has been found,[37] which could hint at differences in catalytic activity between different catalyst types. The difference in the local Ni and Fe coordination we find could be interpreted as a phase separation into Ni- and Fe-rich phases, however considering that i) there is a significant deviation from the pure parent phase coordination, and ii) the mutual influence of the two metals on the local coordination, it is more likely that the material is macroscopically homogeneous, at least at low T_{anneal}. At high T_{anneal} this argument for homogeneity does not hold anymore, since XRD diffraction peaks associated with both α-Fe_2O_3 and NiO are found in some of the mixed metal oxides (Fig. 1), indicating a (partial) spatial phase separation into Fe- and Ni-dominated nanodomains with increasing annealing temperature. EXAFS parameters of these samples are closer to pure oxide values, thus supporting the notion of a spatial phase separation.

XANES linear combination fitting and XANES edge position of the Fe edge spectra suggest a Fe_3O_4-like local environment of all **PO** samples, see Figs. 2 and S7. Our discussion of the electrochromic effect in FeO_x(found in the SI) would suggest a similar interpretation. However, neither shape of the Fourier transform of the EXAFS signal (Fig. S3), nor the EXAFS parameters (Fig. S5) show any sign of Fe_3O_4 characteristics in the Fe edges of the **PO** samples. Considering the Pourbaix diagram for Fe oxides[38] we find the formation of Fe_3O_4 under our electroconditioning unlikely. One possible explanation is that washing the samples after electroconditioning in water causes the reduction of Fe and apparent formation of Fe_3O_4. This interpretation is suported by the Pourbaix diagram, as pH 7 at 0 V is close to the Fe^{2+}/Fe^{3+} transition. However,

we cannot reconciliate this interpreation with the lack of evidence for a Fe_3O_4-like structure in EXAFS and therefore will abstain from further interpretation of the **PO** results. This example serves to illustrate the difficulty of using *post-operando* methods to determine catalytic processes.

Electrochemical activity

Four electrons need to be transferred during the OER. It has been pointed out that a single two-electron transfer reaction is statistically unlikely,[39] therefore most proposed reaction mechanisms consist of four or more distinct reaction steps.[40] Ultimately, only two of these steps determine the catalytic performance: the rate-determining step (RDS) and the potential-determining step (PDS), which are the reaction steps with the slowest kinetics and the highest thermodynamic potential, respectively. While often implicitly or explicitly used as synonyms, the RDS and PDS are necessarily the same reaction step.[39] Determining these reaction steps would provide insight into the reaction mechanism and provide new avenues for catalyst improvement. However, experimental access to these reaction steps is not straightforward. To gain insight into their catalytic properties, we electrochemically benchmark our (Ni,Fe)O_x annealing series by measuring η at catalytic onset and at at 10 mA cm^{-2}, as well as the Tafel slope.

The catalytic onset potential is a measure for the activation potential of the PDS (assuming constant film and series resistance),[25] but does not tell us which step it is. Likewise, the value of the Tafel slope is correlated to the RDS, sequence of RDS and PDS, and reaction intermediary coverage.[41,42] But in itself the Tafels slope cannot reveal the RDS and is therefore often used as a phenomenological descriptor of catalytic activity, *i.e.* how much does the potential have to be increased to increase current density by one order of magnitude. η at 10 mA cm^{-2} does not directly correlate to the reaction mechanism, but is a measure of catalytic efficiency under technologically relevant conditions in solar-driven electrolysis.[43] On their own these observables do not allow for much interpretation, but taken together they provide insights into the catalytic mechanism, especially when combined with structural information and annealing-

induced evolution.

We find a strong decrease of η_{onset} in the **AP** samples from 250 mV for **Ni_{100}-AP** to approximately 125 mV for **$Fe_{75}Ni_{25}$-AP**; this value continuously decreases with increasing Ni content to approximately 100 mV for **Ni_{100}-AP**. In other words, the onset potential of *a*-FeO_x decreases dramatically with even a small inclusion of Ni (≈10 %),[12] and then decreases marginally with further Ni addition. This could be caused by either a change in film resistance R_{film}, or a change in the catalytic process. We measure electrochemical impedance spectroscopy (EIS) under catalytic conditions (1.7 V vs. RHE) to determine R_{film} (see Fig. S10a) and find that R_{film} increases dramatically as soon as Ni is introduced into *a*-FeO_x, and then decreases again with Ni content. Because of the opposite behavior of R_{film} in the initial decrease of η_{onset} we conclude that the OER activation energy decreases with the introduction of Ni. However, with further increase in Ni content the continuous reduction in η at onset is due to a decrease in R_{film}.

We now turn to the behavior of η_{onset} with annealing. While η_{onset} stays approximately constant with T_{anneal} in the **Fe_{100}** series, it increases with T_{anneal} in all Ni containing samples. This increase approximately occurs at the respective phase transition temperature in all mixed metal oxides and the pure NiO_x series, as is shown in Fig. 5a. Again this could be caused by an increase in R_{film}; however EIS results show that R_{film} is constant or trends downward with increasing T_{anneal} in all series (Fig. S10a.). Therefore the increase in onset overpotential with T_{anneal} of all Ni-containing samples must be correlated to an increase in OER activation potential. And since this increase of activation potential occurs at the respective Ni environment transition temperatures for all Ni containing samples it is likely that it is caused by the same change in reaction mechanism, as discussed previously.[25]

The Tafel slopes decrease dramatically for the mixed metal oxides, compared to the single-component oxides, corresponding to a significant increase in catalytic activity, which has ignited the interest in (Ni,Fe)O_x catalysts in the first place.[32] Even small amounts of Fe in NiO_x catalysts improve the reaction kinetics significantly[24,37] and we indeed find a decrease from 100 mV dec^{-1} for **Ni_{100}-AP** to ≈40 mV dec^{-1} for all mixed metal oxide **AP** samples, for which

sample composition does not significantly influence the Tafel slope. With annealing, the Tafel slope of all mixed metal oxides increases starting at $T_{\text{anneal}} \geq 400$ °C which we have identified as the Fe phase transition temperature (*vide supra*). This correlation is illustrated in Fig. 5b. At high T_{anneal} the mixed metal oxide kinetics are similar to pure oxide kinetics, which could point to a interruption of the synergistic catalytic effects between Ni and Fe.

Dual-site mechanism

Recently, a study of Ni and Fe atoms in a polymeric carbon nitride matrix, supported by DFT calculations[44] suggested an OER mechanism where the adsorption of different reaction intermediaries occurs at different sites, due to a site-specific affinity for a certain reaction intermediate. For example, *O and *OH intermediates are more easily adsorbed on Fe sites, while the *OOH intermediary prefers the Ni site. The first two steps of the OER occur at a Fe active site; when a (Fe)*OOH intermediate forms it transfers to a neighboring Ni site, which is the active site for the remainder of the OER cycle. This synergistic explanation is attractive for the catalytic activity in our (Ni,Fe)O_x system, as it could explain why the reaction kinetics (governed by the RDS) change while the PDS stays the same compared to the NiO_x series.[25] Several similar dual-site mechanisms have been proposed for (Ni,Fe)O_x systems.[14–16] Furthermore, such a dual-site mechanism would explain why studies focusing on reaction kinetics predominantly identify Fe as the catalytically active site,[17–20] while studies of the reaction thermodynamics generally attribute catalytic activity to Ni sites or emphasize the importance of Ni sites beyond being just a host material.[21–23]

Our experimental findings can be summed up as follows: i) the onset overpotential of all mixed metal oxides shows the same T_{anneal} dependence as the $\mathbf{Ni_{100}}$ series; ii) the onset overpotential increases at the respective T_{anneal} associated with the Ni environment phase transition; iii) the Tafel slope decreases significantly with incorporation of Fe; and iv) the Tafel slope of the mixed metal oxides increases at the respective T_{anneal} associated with the Fe environment phase transition. While i) and ii) are measures of the PDS and would indicate a Ni active site,

iii) and iv) support the notion of a Fe active site determining the RDS. The only explanation that satisfactorily combines those two apparently contradicting conclusions is the existence of a dual-site mechanism with the PDS occurring at a Ni site and the RDS at a Fe site.

We now examine that mechanism more closely. By integrating the charge passed under the pre-catalytic wave ($Ni^{2+/3+}$ oxidation peak) in the CVs, we can determine the 'steady state' NiOOH population in our catalysts (Fig. S10c). For ease of comparison, the NiOOH populations are normalized to the **Ni_{100}-AP** sample. We find that the NiOOH population decreases linearly with increasing T_{anneal} for the **Ni_{100}** series, but decreases to approximately zero in a sharp stepwise fashion around a T_{anneal} of 350~400 °C for the mixed metal oxides. This step-like evanescence of initial NiOOH coincides with the increase in Tafel slopes, leading us to believe in the involvement of 'steady state' NiOOH in the highly active OER mechanism for our (Ni,Fe)O_x annealed at low T_{anneal}.

Following this argument that the Ni sites govern reaction thermodynamics and Fe sites reaction kinetics, one could speculate that reaction kinetics (as described by the Tafel slope or overpotential at 10 mA cm^{-2}, (*c.f.* Figs. 4 a.-b.) would follow the same trend as the **Fe_{100}** series with T_{anneal}. However, this is clearly not the case as the mixed metal oxides significantly outperform the pure FeO_x catalyst. Thus, the incorporated Ni must significantly alter the catalytic properties of the Fe site. More specifically, the original PDS in **Fe_{100}** gets presumably replaced by an intermediate reaction step at a NiOOH site in the mixed metal oxides; the RDS either occurs at a different reaction step, or gets significantly altered. In pure NiO_x catalysts we found a correlation between a strain in the coordination structure and increased catalytic activity[25] and we find a significantly altered second shell Fe coordination environment in our (Ni,Fe)O_x samples, i.e. an increase in $R_{\text{Fe-M}}$ compared to the value for pure FeO_x (Fig.3). These increased Fe-M bond distances could be indicative of a more $Fe(OH)_2$-like environment.[35] We speculate that this more $Fe(OH)_2$-like coordination could prove beneficial for the adsorption of a *OH reaction intermediate species. Thus, it is conceivable that this strained coordination could be responsible for the increased catalytic activity. Similarly, we find that Fe influences the Ni co-

ordination, and thus presumably the *OOH intermediate affinity, as shown by electrochromic measurements (Fig. S11), where the incorporation of Fe causes the NiOOH population to decrease.

At high T_{anneal} the mixed metal oxide catalyst performance is similar to the performance of either pure metal catalyst, *i.e.* the synergistic effects of Ni and Fe is greatly reduced, if not completely absent. While it is certainly possible that the structural changes to a more crystalline, less strained structure could be the cause for this, we find it unlikely, considering that the performance of crystalline (Ni,Fe)O_x can be close to our amorphous materials. However, XRD provides a possible hint for an explanation for the decrease in catalytic performance at high T_{anneal}: in the **$Fe_{25}Ni_{75}$** series we detect diffraction peaks corresponding to both the NiO and a α-Fe_2O_3 phase, see Fig. 1, indicating a phase separation between Fe an Ni phases. We do not detect a similar XRD pattern for the Fe-rich **$Fe_{50}Ni_{50}$** or **$Fe_{75}Ni_{25}$** compositions. This does not necessarily mean that there is no spatial separation between Ni and Fe occurring in these series, just that there could be not enough Ni to for a separate Ni phase in the investigated annealing range. A spatial separation between Ni and Fe would suppress a dual-site mechanism, providing an easy explanation for the reduced reaction kinetics that are close to the NiO_x or FeO_x kinetics at high T_{anneal}. A spatially resolved analysis of the catalyst surface could shed light on these speculations, but is beyond the scope of this work.

Summary and conclusions

We have fabricated (Ni,Fe)O_x thin-film OER catalysts, annealed them various temperatures, characterized them structurally by XAS and XRD, and benchmarked their electrochemical properties. We find amorphous-to-amorphous phase transitions in all series. From the Ni K edge XAS, the $Ni(OH)_2$-like coordination transitions to a NiO-like coordination at $T_{\text{anneal}} \approx 250$ °C for **Ni_{100}** and at $T_{\text{anneal}} \approx 400$ °C for the mixed-metal oxides. From the Fe K edge XAS we find a transition from a FeOOH-like coordination to a α-Fe_2O_3-like one at $T_{\text{anneal}} \approx 400$ °C for **Fe_{100}** and

$T_{\text{anneal}} \approx 500$ °C for the mixed metal oxides. XRD diffraction patterns, indicative of long-range order crystallinity, only appear at higher T_{anneal} in all series. Notably, the intermixing of Fe and Ni in the mixed metal oxides stabilizes the amorphous phase, such that XRD peaks are detected at significantly higher T_{anneal} than in either pure metal oxide. This observation could be a hint explaining the stability of (Ni,Fe)$O_x$catalysts under catalytic conditions. The catalytic onset potentials of the mixed metal oxides exhibit similar values to the pure NiO_x series, show a similar increase with T_{anneal}, and most importantly increase at approximately the Ni edge phase transition temperature. Tafel slopes of the mixed metal oxides are significantly lower than either pure metal oxide, indicating superior OER reaction kinetics. With increasing T_{anneal} the Tafel slopes stay approximately constant at a value of around 40 mV dec^{-1} to then increase at the Fe environment phase transition temperature.

From these experimental observations we suggest that reaction thermodynamics are determined by a Ni site, while kinetics are apparently decided at a Fe site. The only mechanism compatible with those two conclusions is a dual-site mechanism, where part of the OER reaction steps occur at a Fe site, and the other part at a neighboring Ni site. Thus, we conclude that the synergistic catalytic performance of (Ni,Fe)O_x catalysts is due to a dual-site mechanism, with the Fe site determining the reaction rate and the Ni site determining the activation potential.

At high annealing temperatures the mixed metal oxides lose their superior catalytic performance, which we speculate to be caused by a phase separation, *i.e.* spatial separation between Ni and Fe, as suggested by XRD results. Such a separation would suppress a dual site mechanism, thus impeding catalytic performance.

This study provides a previously unrecognized correlation between local ordering and catalytic activity in amorphous materials, and provides avenues for new catalyst design and development. Our methodical approach of characterizing the gradual structural evolution and measuring changes in catalytic properties allows us unprecedented insight into the oxygen evolution reaction (OER) mechanism in amorphous (Ni,Fe)O_x catalysts. As a result, we find that the OER must proceed via a dual-site mechanism in this system. Such a mechanism has been the-

oretically suggested, however experimental evidence has been scarce.

In a broader sense, this work provides insight into structure-property relations in amorphous materials, by observing and correlating trends. This methodology can be used as a blueprint for the investigation of other amorphous catalyst materials. Furthermore, the demonstration that amorphous-to-amorphous phase transitions are a general feature of this catalyst system sheds light on a wealth of complexity hitherto under-appreciated. It seams reasonable to suggest that this behavior is very likely much more universal then previously recognized. With the rise of reports on high-activity amorphous catalysts, it becomes self-evident that simply identifying materials as "amorphous" is inadequate and that more in-depth structure-property relationships in amorphous systems are warranted.

Acknowledgements

The authors thank NSERC of Canada (Discovery Grant) for operating funds. This research used facilities funded by the University of Calgary and the Canadian Foundation for Innovation (John R. Evans Leaders Fund). Funding to M.A.W.S. was provided by the Alexander von Humboldt Foundation Feodor Lynen Research Fellowship and the University of Calgary's Global Research Initiative in Sustainable Low Carbon Unconventional Resources funded by the Canada First Research Excellence Fund (CFREF). We thank Emilio Heredia for technical assistance at the BIOXAS beamline. Part or all of the research described in this paper was performed at the Canadian Light Source, a national research facility of the University of Saskatchewan, which is supported by the Canada Foundation for Innovation (CFI), the Natural Sciences and Engineering Research Council (NSERC), the National Research Council (NRC), the Canadian Institutes of Health Research (CIHR), the Government of Saskatchewan, and the University of Saskatchewan.

Author contributions

MAWS, KD, and ST conceived and designed the experiment. MAWS performed UV-vis spectroscopy, electrochemical, and electrochromic measurements. MAWS, ST, OC, SJ, NR, and RC recorded the XAS spectra. MAWS analyzed the data. MAWS and ST wrote the manuscript; all co-authors provided feedback on the manuscript.

Conflict of Interest

There are no conflicts of interest to declare.

Supporting Information

The SI contains experimental methods, UV-Vis spectra, EXAFS spectra and fit parameters, XANES linear combination fitting, oxidation states, electrochemical and electrochromic characterization, and additional supporting references[45–56]

References

(1) Felgenhauer, M.; Hamacher, T. State-of-the-art of commercial electrolyzers and on-site hydrogen generation for logistic vehicles in South Carolina. *Int. J. Hydrog.* **2015**, *40*, 2084 – 2090.

(2) Steward, D.; Saur, G.; Penev, M.; Ramsden, T. Technical Report NREL/TP-560-46719 November 2009 Lifecycle Cost Analysis of Hydrogen Versus Other Technologies for Electrical Energy Storage. *Tech. Rep.* **2009**,

(3) Craig Grimes, S. R., Ooman Varghese, Ed. *Light, Water, Hydrogen*, 1st ed.; Springer US, 2008.

(4) Etzi Coller Pascuzzi, M.; Man, A. J. W.; Goryachev, A.; Hofmann, J. P.; Hensen, E. J. M. Investigation of the stability of NiFe-(oxy)hydroxide anodes in alkaline water electrolysis under industrially relevant conditions. *Catal. Sci. Technol.* **2020**, *10*, 5593–5601.

(5) Gong, M.; Dai, H. A mini review of NiFe-based materials as highly active oxygen evolution reaction electrocatalysts. *Nano Res.* **2015**, *8*, 23–39.

(6) Mohammed-Ibrahim, J. A review on NiFe-based electrocatalysts for efficient alkaline oxygen evolution reaction. *J. Power Sources* **2020**, *448*, 227375.

(7) Wang, C.; Yang, H.; Zhang, Y.; Wang, Q. NiFe Alloy Nanoparticles with hcp Crystal Structure Stimulate Superior Oxygen Evolution Reaction Electrocatalytic Activity. *Angew. Chem. Int. Ed.* **2019**, *58*, 6099–6103.

(8) Feng, Y.; Yu, X.-Y.; Paik, U. N-doped graphene layers encapsulated NiFe alloy nanoparticles derived from MOFs with superior electrochemical performance for oxygen evolution reaction. *Sci. Rep.* **2016**, *6*, 34004.

(9) Wei, P.; Sun, X.; Liang, Q.; Li, X.; He, Z.; Hu, X.; Zhang, J.; Wang, M.; Li, Q.; Yang, H.; Han, J.; Huang, Y. Enhanced Oxygen Evolution Reaction Activity by Encapsulating NiFe Alloy Nanoparticles in Nitrogen-Doped Carbon Nanofibers. *ACS Appl. Mater. Interfaces* **2020**, *12*, 31503–31513, PMID: 32569458.

(10) Bau, J. A.; Li, P.; Marenco, A. J.; Trudel, S.; Olsen, B. C.; Luber, E. J.; Buriak, J. M. Nickel/Iron Oxide Nanocrystals with a Nonequilibrium Phase: Controlling Size, Shape, and Composition. *Chem. Mater.* **2014**, *26*, 4796–4804.

(11) Smith, R. D. L.; Prévot, M. S.; Fagan, R. D.; Trudel, S.; Berlinguette, C. P. Water Oxidation Catalysis: Electrocatalytic Response to Metal Stoichiometry in Amorphous Metal Oxide Films Containing Iron, Cobalt, and Nickel. *J. Am. Chem. Soc.* **2013**, *135*, 11580–11586.

(12) Smith, R. D. L.; Prévot, M. S.; Fagan, R. D.; Zhang, Z.; Sedach, P. A.; Siu, M. K. J.; Trudel, S.; Berlinguette, C. P. Photochemical Route for Accessing Amorphous Metal Oxide Materials for Water Oxidation Catalysis. *Science* **2013**, *340*, 60–63.

(13) Lei, L.; Huang, D.; Zhou, C.; Chen, S.; Yan, X.; Li, Z.; Wang, W. Demystifying the active roles of NiFe-based oxides/(oxy)hydroxides for electrochemical water splitting under alkaline conditions. *Coord. Chem. Rev.* **2020**, *408*, 213177.

(14) Xiao, H.; Shin, H.; Goddard, W. A. Synergy between Fe and Ni in the optimal performance of (Ni,Fe)OOH catalysts for the oxygen evolution reaction. *Proc. Natl. Acad. Sci. U.S.A* **2018**, *115*, 5872–5877.

(15) Qiu, Z.; Tai, C.-W.; Niklasson, G. A.; Edvinsson, T. Direct observation of active catalyst surface phases and the effect of dynamic self-optimization in NiFe-layered double hydroxides for alkaline water splitting. *Energy Environ. Sci.* **2019**, *12*, 572–581.

(16) Song, F.; Busch, M. M.; Lassalle-Kaiser, B.; Hsu, C.-S.; Petkucheva, E.; Bensimon, M.; Chen, H. M.; Corminboeuf, C.; Hu, X. An Unconventional Iron Nickel Catalyst for the Oxygen Evolution Reaction. *ACS Cent. Sci.* **2019**, *5*, 558–568.

(17) Bates, M. K.; Jia, Q.; Doan, H.; Liang, W.; Mukerjee, S. Charge-Transfer Effects in Ni–Fe and Ni–Fe–Co Mixed-Metal Oxides for the Alkaline Oxygen Evolution Reaction. *ACS Catal.* **2016**, *6*, 155–161.

(18) Dionigi, F. et al. In-situ structure and catalytic mechanism of NiFe and CoFe layered double hydroxides during oxygen evolution. *Nat. Comm.* **2020**, *11*, 2522.

(19) H.B., H. B. W. J. G. Iron Is the Active Site in Nickel/Iron Water Oxidation Electrocatalysts. *Molecules* **2018**, 903.

(20) Ahn, H. S.; Bard, A. J. Surface Interrogation Scanning Electrochemical Microscopy of

Ni1–xFexOOH (0 < x < 0.27) Oxygen Evolving Catalyst: Kinetics of the "fast" Iron Sites. *J. Am. Chem. Soc.* **2016**, *138*, 313–318, PMID: 26645678.

(21) Vandichel, M.; Laasonen, K.; Kondov, I. Oxygen Evolution and Reduction on Fe-doped NiOOH: Influence of Solvent, Dopant Position and Reaction Mechanism. *Top. Catal.* **2020**, 833–845.

(22) Li, N.; Bediako, D. K.; Hadt, R. G.; Hayes, D.; Kempa, T. J.; von Cube, F.; Bell, D. C.; Chen, L. X.; Nocera, D. G. Influence of iron doping on tetravalent nickel content in catalytic oxygen evolving films. *Proc. Natl. Acad. Sci. U.S.A* **2017**, *114*, 1486–1491.

(23) Trześniewski, B. J.; Diaz-Morales, O.; Vermaas, D. A.; Longo, A.; Bras, W.; Koper, M. T.; Smith, W. A. In Situ Observation of Active Oxygen Species in Fe-Containing Ni-Based Oxygen Evolution Catalysts: The Effect of pH on Electrochemical Activity. *J. Am. Chem. Soc.* **2015**, *137*, 15112–15121, PMID: 26544169.

(24) Stevens, M. B.; Trang, C. D. M.; Enman, L. J.; Deng, J.; Boettcher, S. W. Reactive Fe-Sites in Ni/Fe (Oxy)hydroxide Are Responsible for Exceptional Oxygen Electrocatalysis Activity. *J. Am. Chem. Soc.* **2017**, *139*, 11361–11364, PMID: 28789520.

(25) Schoen, M. A. W.; Randell, N. M.; Calderon, O.; Jimenez Villegas, S.; Thomson, Z.; Chernikov, R.; Trudel, S. Structural Evolution in Photodeposited Nickel (oxy)hydroxide Oxygen Evolution Electrocatalysts. *ACS Appl. Energy Mater.* **2020**, *XXX*, 10.1021/acsaem.0c02383.

(26) Trudel, S.; Crozier, E. D.; Gordon, R. A.; Budnik, P. S.; Hill, R. H. X-ray absorption fine structure study of amorphous metal oxide thin films prepared by photochemical metalorganic deposition. *J. Solid State Chem.* **2011**, *184*, 1025 – 1035.

(27) Smith, R. D. L.; Pasquini, C.; Loos, S.; Chernev, P.; Klingan, K.; Kubella, P.; Mohammadi, M. R.; Gonzalez-Flores, D.; Dau, H. Spectroscopic identification of active sites for the oxygen evolution reaction on iron-cobalt oxides. *Nat. Comm.* **2017**, *8*, 2022.

(28) Kurzman, J. A.; Dettelbach, K. E.; Martinolich, A. J.; Berlinguette, C. P.; Neilson, J. R. Structural Characteristics and Eutaxy in the Photo-Deposited Amorphous Iron Oxide Oxygen Evolution Catalyst. *Chem. Mater.* **2015**, *27*, 3462–3470.

(29) Zhang, C.; Berlinguette, C. P.; Trudel, S. Water oxidation catalysis: an amorphous quaternary Ba-Sr-Co-Fe oxide as a promising electrocatalyst for the oxygen-evolution reaction. *Chem. Commun.* **2016**, *52*, 1513–1516.

(30) Zhang, C.; Fagan, R. D.; Smith, R. D. L.; Moore, S. A.; Berlinguette, C. P.; Trudel, S. Mapping the performance of amorphous ternary metal oxide water oxidation catalysts containing aluminium. *J. Mater. Chem. A* **2015**, *3*, 756–761.

(31) Zhang, C.; Zhang, X.; Daly, K.; Berlinguette, C. P.; Trudel, S. Water Oxidation Catalysis: Tuning the Electrocatalytic Properties of Amorphous Lanthanum Cobaltite through Calcium Doping. *ACS Catalysis* **2017**, *7*, 6385–6391.

(32) Corrigan, D. A. The Catalysis of the Oxygen Evolution Reaction by Iron Impurities in Thin Film Nickel Oxide Electrodes. *J. Electrochem. Soc.* **1987**, *134*, 377–384.

(33) Trudel, S.; Li, G.; Zhang, X.; Hill, R. H. Positive and Negative Lithography by Photochemical Metalorganic Deposition from Metal 2-ethylhexanoates. *J. Photopolym. Sci. Tec.* **2006**, *19*, 467–475.

(34) Wilke, M.; Farges, F.; Petit, P.-E.; Brown, J., Gordon E.; Martin, F. Oxidation state and coordination of Fe in minerals: An Fe K-XANES spectroscopic study. *Am. Mineralogist* **2001**, *86*, 714–730.

(35) Friebel, D.; Louie, M. W.; Bajdich, M.; Sanwald, K. E.; Cai, Y.; Wise, A. M.; Cheng, M.-J.; Sokaras, D.; Weng, T.-C.; Alonso-Mori, R.; Davis, R. C.; Bargar, J. R.; Nørskov, J. K.; Nilsson, A.; Bell, A. T. Identification of Highly Active Fe Sites in (Ni,Fe)OOH for Electrocatalytic Water Splitting. *J. Am. Chem. Soc.* **2015**, *137*, 1305–1313.

(36) Smith, R. D. L.; Pasquini, C.; Loos, S.; Chernev, P.; Klingan, K.; Kubella, P.; Mohammadi, M. R.; González-Flores, D.; Dau, H. Geometric distortions in nickel (oxy)hydroxide electrocatalysts by redox inactive iron ions. *Energy Environ. Sci.* **2018**, *11*, 2476–2485.

(37) Dionigi, F.; Strasser, P. NiFe-Based (Oxy)hydroxide Catalysts for Oxygen Evolution Reaction in Non-Acidic Electrolytes. *Adv. Ener. Mat.* **2016**, *6*, 1600621.

(38) Beverskog, B.; Puigdomenech, I. Revised pourbaix diagrams for iron at 25–300 °C. *Corr. Sci.* **1996**, *38*, 2121 – 2135.

(39) Koper, M. T. M. Analysis of electrocatalytic reaction schemes: distinction between rate-determining and potential-determining steps. *J. Solid State Electrochem.* **2013**, *17*, 339–344.

(40) Fabbri, E.; Schmidt, T. J. Oxygen Evolution Reaction—The Enigma in Water Electrolysis. *ACS Catal.* **2018**, *8*, 9765–9774.

(41) Bockris, J. O. M.; Otagawa, T. The Electrocatalysis of Oxygen Evolution on Perovskites. *J. Electrochem. Soc.* **1984**, *131*, 290–302.

(42) Shinagawa, T.; Garcia-Esparza, A. T.; Takanabe, K. Insight on Tafel slopes from a microkinetic analysis of aqueous electrocatalysis for energy conversion. *Sci. Rep.* **2015**, *5*, 13801.

(43) Surendranath, Y.; Bediako, D. K.; Nocera, D. G. Interplay of oxygen-evolution kinetics and photovoltaic power curves on the construction of artificial leaves. *Proc. Natl. Acad. Sci. U.S.A.* **2012**, *109*, 15617–15621.

(44) Wu, C.; Zhang, X.; Xia, Z.; Shu, M.; Li, H.; Xu, X.; Si, R.; Rykov, A. I.; Wang, J.; Yu, S.; Wang, S.; Sun, G. Insight into the role of Ni–Fe dual sites in the oxygen evolution reaction based on atomically metal-doped polymeric carbon nitride. *J. Mater. Chem. A* **2019**, *7*, 14001–14010.

(45) Trotochaud, L.; Young, S. L.; Ranney, J. K.; Boettcher, S. W. Nickel–Iron Oxyhydroxide

Oxygen-Evolution Electrocatalysts: The Role of Intentional and Incidental Iron Incorporation. *J. Am. Chem. Soc.* **2014**, *136*, 6744–6753.

(46) Patterson, A. L. The Scherrer Formula for X-Ray Particle Size Determination. *Phys. Rev.* **1939**, *56*, 978–982.

(47) Langford, J. I.; Wilson, A. J. C. Scherrer after sixty years: A survey and some new results in the determination of crystallite size. *J. Appl. Crystallogr.* **1978**, *11*, 102–113.

(48) Tauc, J. Optical properties and electronic structure of amorphous Ge and Si. *Mater. Res. Bull.* **1968**, *3*, 37 – 46.

(49) Ravel, B.; Newville, M. *ATHENA*, *ARTEMIS*, *HEPHAESTUS*: data analysis for X-ray absorption spectroscopy using *IFEFFIT*. *J. Synchrotron Radiat.* **2005**, *12*, 537–541.

(50) Kraft, S.; Stümpel, J.; Becker, P.; Kuetgens, U. High resolution x-ray absorption spectroscopy with absolute energy calibration for the determination of absorption edge energies. *Rev. Sci. Instrum.* **1996**, *67*, 681–687.

(51) Mustre de Leon, J.; Rehr, J. J.; Zabinsky, S. I.; Albers, R. C. Ab initio curved-wave x-ray-absorption fine structure. *Phys. Rev. B* **1991**, *44*, 4146–4156.

(52) Rehr, J. J.; Albers, R. C. Scattering-matrix formulation of curved-wave multiple-scattering theory: Application to x-ray-absorption fine structure. *Phys. Rev. B* **1990**, *41*, 8139–8149.

(53) Klaus, S.; Cai, Y.; Louie, M. W.; Trotochaud, L.; Bell, A. T. Effects of Fe Electrolyte Impurities on $Ni(OH)_2$/NiOOH Structure and Oxygen Evolution Activity. *J. Phys. Chem. C* **2015**, *119*, 7243–7254.

(54) Monk, P.; Mortimer, R.; Rosseinsky, D. *Electrochromism and Electrochromic Devices*; Cambridge University Press, 2007.

(55) Kadam, L.; Patil, P. Studies on electrochromic properties of nickel oxide thin films prepared by spray pyrolysis technique. *Sol. Energy Mater Sol.* **2001**, *69*, 361 – 369.

(56) Garcia-Lobato, M.; Martinez, A. I.; Perry, D. L.; Castro-Roman, M.; Zarate, R.; Escobar-Alarcon, L. Elucidation of the electrochromic mechanism of nanostructured iron oxides films. *Sol. Energy Mater Sol. Cells* **2011**, *95*, 751 – 758.

Table of content graphic

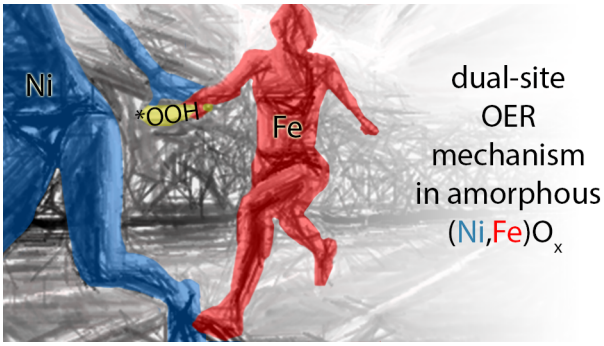

Electronic Supplementary Information. Local structural changes in polyamorphous (Ni,Fe)O_x electrocatalysts suggest a dual-site oxygen evolution reaction mechanism

Martin A. W. Schoen,[a] Oliver Calderon,[a] Nicholas Randell,[a] Santiago Jimenez Villegas,[a] Katelynn M. Daly,[a] Roman Chernikov,[b] and Simon Trudel*[a‡]

[a] *Department of Chemistry, University of Calgary, 2500 University Dr NW, Calgary, AB, Canada.*

[b] *Canadian Light Source, Saskatoon, SK, Canada.*

⋆ E-mail: trudels@ucalgary.ca

Experimental details

Chemicals and Materials

Ni(II) 2-ethylhexanoate (**Ni(2-ethex)$_2$**, 78 % in mineral spirits) and Fe(II) 2-ethylhexanoate (**Fe(2-ethex)$_3$**, 50 % in mineral spirits) were purchased from STREM Chemicals; methyl isobutyl ketone (MIBK) was purchased from Alpha Aesar; potassium hydroxide was obtained from EMD Millipore. All were used as-receievd without further purification. NiO, $Ni(OH)_2$, α-Fe_2O_3, FeOOH, and Fe_3O_4 crystalline powders used as standard reference compounds for XRD, XANES, and EXAFS was purchased from Alpha Aesar. Fluorine-doped tin oxide (7 Ω / $sq.$) on glass substrates (FTO) were acquired from Hartford Glass Company. FTO substrates were cleaned by 5 minute sonication in acetone, which was not allowed to dry and rinsed off with isopropanol and subsequently dried in N_2. SiO_2 (50 nm) / Si subtrates were prepared by cleaning in-house cut Si(100) wafers (Universiy Wafers, B-doped, 500 μm thick), using the same cleaning procedure as for the FTO substrates. A thermal oxide layer of approximately 50 nm thickness was produced by heating the silicon chips in air for 5 h at 1000 °C. Fe-free KOH electrolye solution was prepared following previously reported methods.[25,45]

Thin film fabrication

Amorphous NiO_x, FeO_x, and (Ni,Fe)O_x films were deposited by ultraviolet-initiated photochemical deposition, as previously reported.[26,33] Briefly, **Ni(2-ethex)$_2$** and **Fe(2-ethex)$_3$** were combined at the target Fe-to-Ni molar ratio, and diluted to 15 total precursor wt% in MIBK. The resulting precursor solution was then spin coated (Laurel, 3000 rpm, 60 s) on clean FTO substrates (FTO) or SiO_2(50 nm)/Si substrates. These films were then irradiated with UV light (Atlantic UV lamp model, λ = 185 nm and 254 nm) for 24 h, ensuring a complete decomposition of the ligands, producing a uniform thin film. The films were used as-prepared (no anneal), or annealed at temperatures ranging between 100 and 600 °C for samples on FTO substrates, and up to 1000 °C for samples on Si substrates (the latter were used for XRD).

X-ray diffraction (XRD)

XRD was performed with a Bruker D8 Advance Eco with a Cu K_α tube (λ = 1.5406 Å) in the vicinity of the (111) and (200) peaks for NiO and (104) and (110) peaks of α-Fe_2O_3 (2θ = 32 - 46 °, step width 0.04°, and 3 s averaging per step). The crystallite size d_{cr} was estimated using the Scherrer equation[46]

$$d_{cr} = \frac{K\lambda}{\beta \cos\theta}, \tag{S1}$$

where K is the shape factor (a value of 0.9 was used), λ is the x-ray wavelength, β is the instrument-broadening corrected full width at half maximum (FWHM) of the XRD peak, and θ is the Bragg angle. The XRD peak is fitted with a Lorentzian function to extract the peak's FWHM. The FWHM is corrected for instrument broadening, which is determined as the FWHM of a bulk powdered NiO (α-Fe_2O_3) sample (β=FWHM(measured)-FWHM(NiO/α-Fe_2O_3 powder)). For two diffraction peaks occurring in a spectrum, the reported d_{cr} is an average over both peaks. For **$Fe_{25}Ni_{25}$**, both NiO and α-Fe_2O_3 crystallite sizes are reported. Error bars are estimated from the 2σ confidence interval of the Lorentzian fits with an additional 10 % error from the uncertainty in shape factor K which typically ranges from 0.8 to 1 for similar samples.[47]

Ultraviolet-visible (UV-vis) spectroscopy

UV-vis spectroscopy was performed with a Cary 5000 spectrometer equipped with a DRA-2500 diffuse reflectance attachment between 0.6 eV and 5 eV. The obtained spectra were analyzed with the Tauc method[48] to obtain the band gap. Errors are estimated from 2σ confidence intervals of the linear fit to the Tauc plot.

X-ray absorption spectroscopy (XAS)

XAS at the Ni and Fe K edges were collected at the BioXAS beamline of the Canadian Light Source. A Si(220) double crystal monochromator was used and second harmonic rejection was

done by a double-bounce harmonic rejection (DBHR) mirror with CVD diamond coating. X-ray fluorescence spectra were recorded with a 32-channel energy-discriminating Canberra Ge fluorescence detector. Ni and Fe reference foil spectra were taken before measuring an edge series to determine the energy offset. Sample spectra were acquired from 150 eV below the absorption edge to $k = 14$ Å^{-1}.

Two series of samples were measured: annealed (Ni,Fe)O_x films without further treatment; and a series of corresponding electrochemically treated films, measured *post-operando*, labelled **PO**. For the **PO** series the samples were put in the electrochemical cell (described below in Section) and held at a potential of 1.9 V vs. RHE ($\approx$ 15mA/cm^2) for 120 s, rinsed, dried off, and measured *ex-situ*. Samples were measured within 3 h of electrochemical treatment, since visible discoloration of the treated samples occurred after 8 h in ambient conditions.

Additionally, spectra of powdered NiO, $Ni(OH)_2$, α-Fe_2O_3, Fe_3O_4, and FeOOH were recorded as comparative reference spectra.

All spectra were analyzed using the Demeter software package version 0.9.26[49] after normalization of the edge jump and flattening. The energy was calibrated using the absolute energy list by Kraft,[50] using Fe and Ni foils. The following data processing settings were used: pre-edge range -150 eV to -50 eV, normalization range 200 eV to 700 eV, $R_{\mathrm{bkg}} = 1.1$ Å, spline range k = 0-14 Å^{-1}, and Fourier transform in k from 3 to 12 Å^{-1}. Scattering paths were calculated using FEFF6[51,52] based on a structural model of NiO for the Ni edges and a simple two-shell model for the Fe edges. Fits are weighted k and k^3. Error bars for the extracted parameters are the standard errors calculated by Artemis.

Electrochemistry

Electrochemical measurements were carried out using a CH Instruments 660D potentiostat. A Pt mesh was used as a counter electrode and a saturated Ag/AgCl electrode used as a reference electrode, sitting in a Luggin cappillary. The supporting electrolyte is 1 M KOH aqueous solution. Fe-free KOH was used for the $\mathbf{Ni}_{100}$ series to avoid electrolyte impurities in the films.[45,53]

Calibration of the Ag/AgCl (sat. KCl) electrode against a 1 mM aqueous solution of $Na_4[Fe(CN)_6]$ (E = 0.361 V vs. NHE) was regularly performed throughout the study thus obtaining potential vs./ NHE. The iR-correcetd overpotential η is calculated[11] as:

$$\eta = E_{\text{applied vs./ NHE}} + 0.059 \cdot \text{pH} - 1.23 - iR \tag{S2}$$

All measurements are reported as current densities, normalized by the geometric surface area. Unless specified otherwise, all potentials are against the reverbersible hydrogen electrode (RHE). As indicated, all overpotentials η are iR-corrected.

Cyclic voltammetry (CV) was carried out at a sweep rate of 0.01 V s^{-1}. CVs were run until the catalyst was stable. η at catalytic onset and at a current density of 10 mA cm^{-2} were then determined. Catalytic onset was defined as the start of the Tafel region. Step-wise voltammetry was carried out in the linear Tafel region. At each step the catalyst was given 40 s to stabilize before measuring. The Tafel slope was then extracted from the linear section of the log(j) vs. η plot. All electrochemical measurements were measured in triplicate and reported values are the average of these measurements. Errors are estimated from the standard deviation of the triplicate results.

Electrochemical impedance spectroscopy (EIS) was performed at a potential of 1.7 V vs. RHE at frequencies between 10^6 to 10^{-2} Hz with 10 points per decade. Spectra were analyzed by the Zview 2 software (Ametek Scientific Instruments) by modelling the data by an equivalent circuit consisting of two constant phase elements (CPEs) and tree resistors, compare Scheme S1. The two CPEs are each in parallel with one resistor, thus modelling the film capacitance and resistance, as well as the double layer capacitance and charge transfer resistance. The third resistor in series is used to model the circuit's series resistance. EIS fit parameters for the mixed metal oxides and pure FeO_xseries can be found in S5. The equivalent circuit and for parameters for the NiO_xseries can be found in Ref.[25]

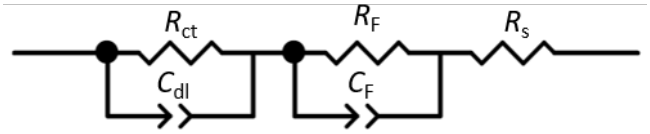

Figure S1: Scheme of the equivalent circuit for EIS data analysis. Elements of the circuit are double layer capacitance C_{dl}, charge transfer resistance R_{ct}, film resistance R_{film}, film capacitance C_{film}, and series resistance R_s

Electrochromism

Samples were measured *in-situ* submerged in a 1 M KOH solution in a quartz cuvette, with the Pt mesh counter electrode and Ag/AgCl(sat'd) reference electrode submerged in the cuvette and an adjacent Luggin capillary, respectively. Spectra in the visible range (350 nm to 800 nm) were taken in the following order: before applying a current, after running approx. 10 CVs (0.9 V to 2.4 V vs./ RHE at 0.1 and 0.01 V s^{-1}), at the potential of the first oxidation peak, at 1.9 V vs./ RHE, at 2.4 V vs./ RHE, at open current potential, and after running a regeneration cycle. 100 % transmission for these measurements was defined as the transmission of the KOH-filled quartz cuvette. Regeneration cycles consisted of 3 CVs from 0.9 to 1.1 V vs./ RHE at 0.01 V s^{-1}, recovering maximal transmission after applying the potential.

Kinetic measurement were taken by measuring transmission over time at 450 nm and applying a single voltage step of 2.4 V vs./ RHE and turning off the potential once a steady state is achieved. Similarly, transmission is measured during CVs from 0.9 to 2.4 V vs./ RHE at 0.01 V s^{-1}.

Supporting plots and results

UV-VIS and band gap

Tauc plots and resulting band gaps for all measured samples are plotted in Fig. S2.

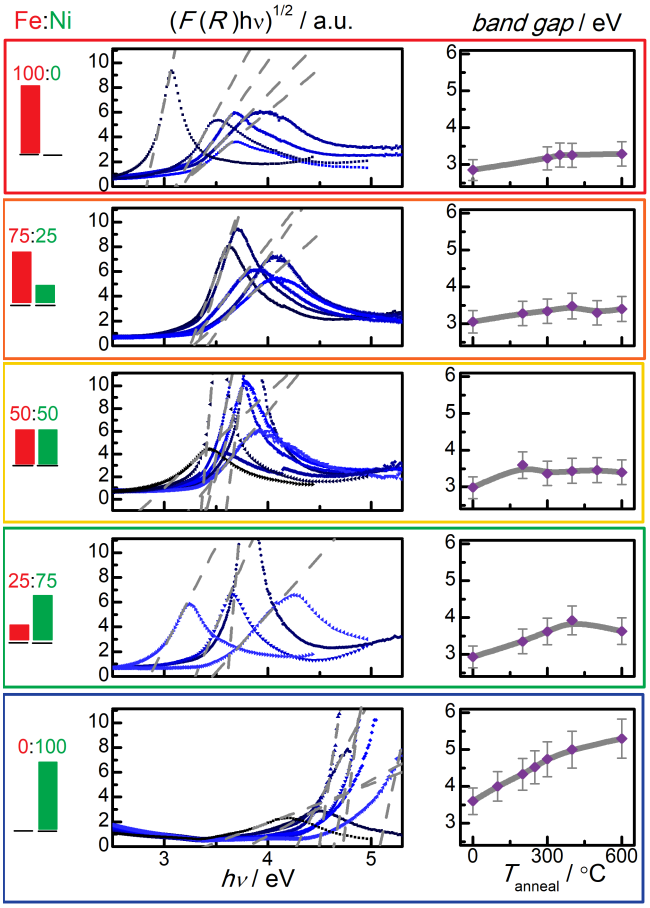

Figure S2: Tauc plots for UV-Vis diffuse reflectance spectra (left-column panels) with fits to the data (dashed gray lines) and band gaps with guide-to-the-eye lines (right-column panels) are plotted for sample compositions denoted on the left. In the Tauc plots increasing T_{anneal} is signified by lighter blue data points.

EXAFS

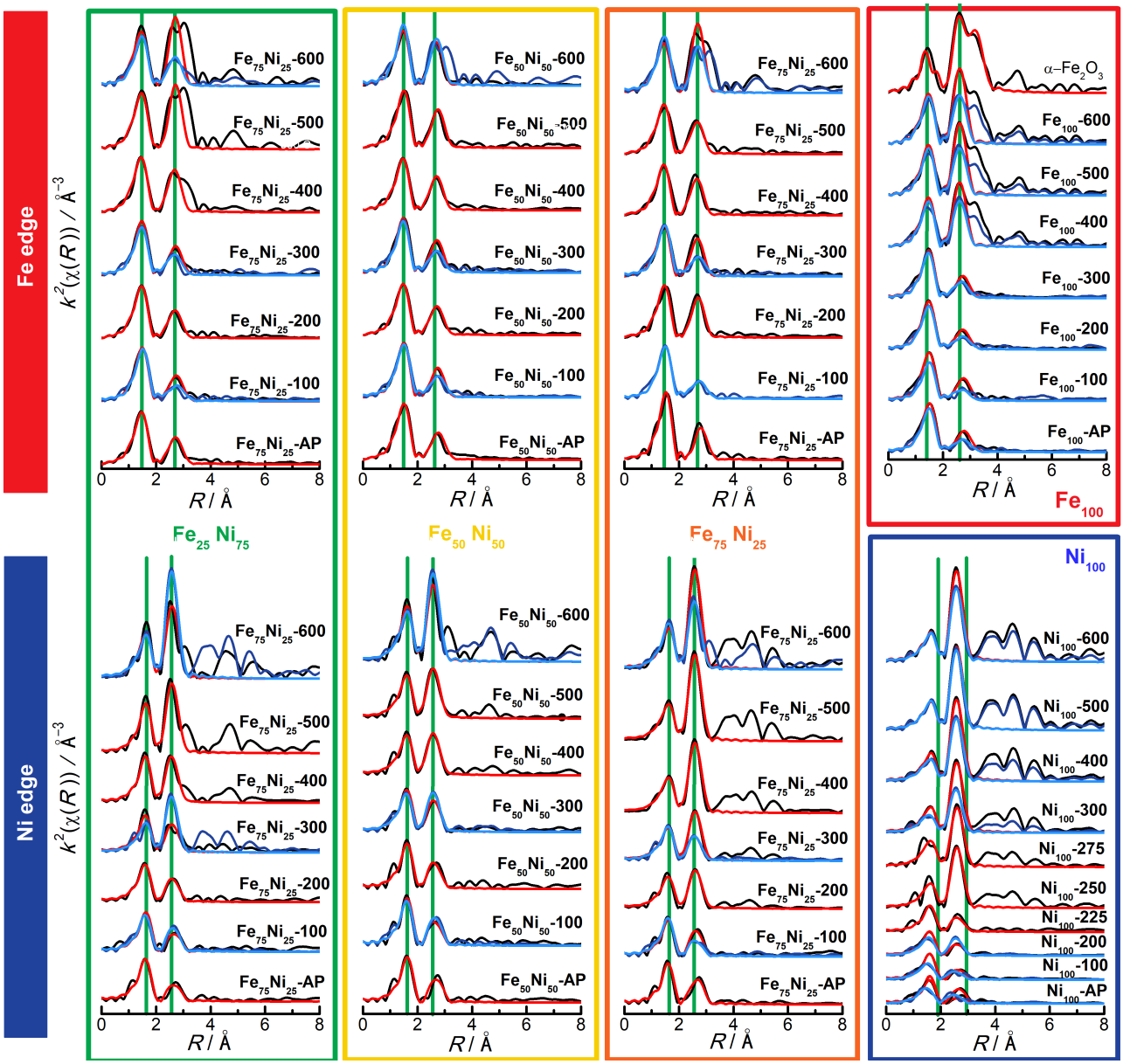

Figure S3: The k^2-weighted Fourier transform of the EXAFS signal, $k^2 \cdot \chi(R)$, is plotted against reduced distance R for Fe (upper row) and Ni K edges (lower row) for sample compositions denoted between the panels. First- and second-shell bond distances of crystaline α-Fe_2O_3 and NiO reference compounds are plotted as vertical lines. Spectra of the annealing series are plotted in black, with models plotted in red. The **PO** series are plotted in dark blue, with models in light blue.

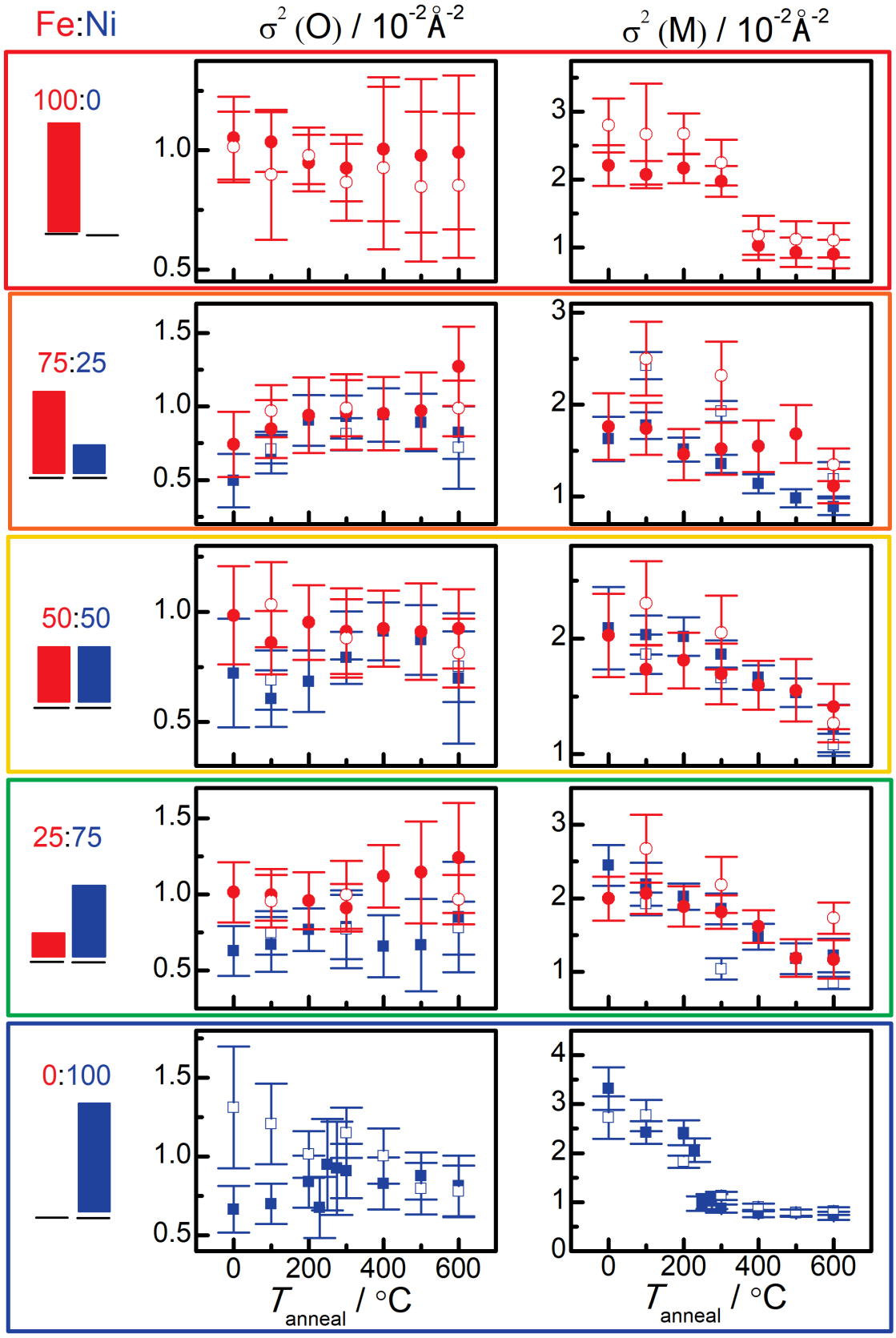

Figure S4: Debye Waller factors are plotted for Ni and Fe first- and second-shell bonds against T_{anneal}. Closed symbols represent the annealing series and open symbols show the data for the **PO** series.

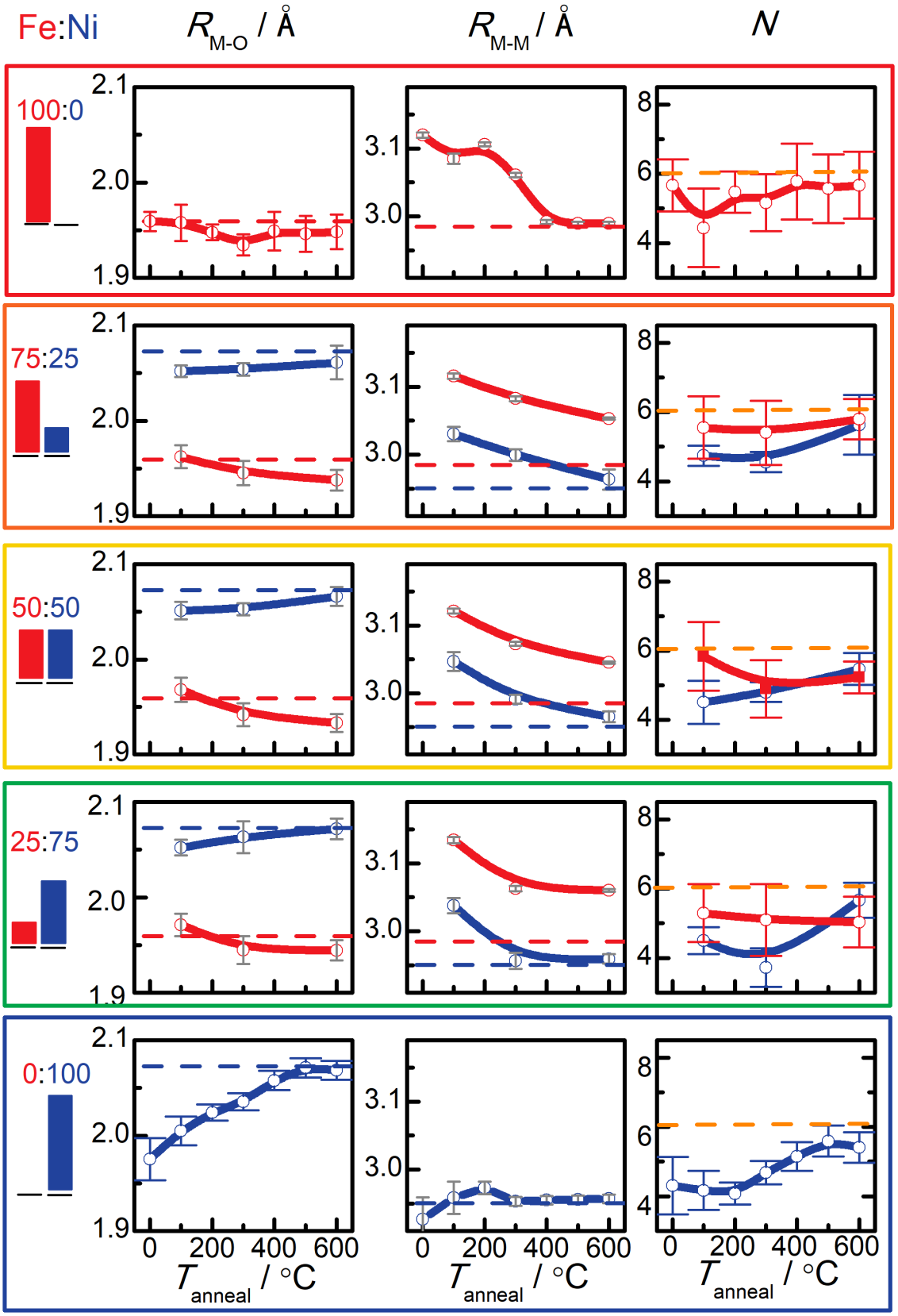

Figure S5: EXAFS fit parameters for the **PO** sample series. Metal-oxygen first-shell and metal-metal second-shell bond distances are plotted in the left and middle columns, respectively; coordination numbers N in the right column. Ni edge parameters are plotted in blue open symbols and Fe edge parameters in red open symbols. Lines are guides to the eye.

XANES

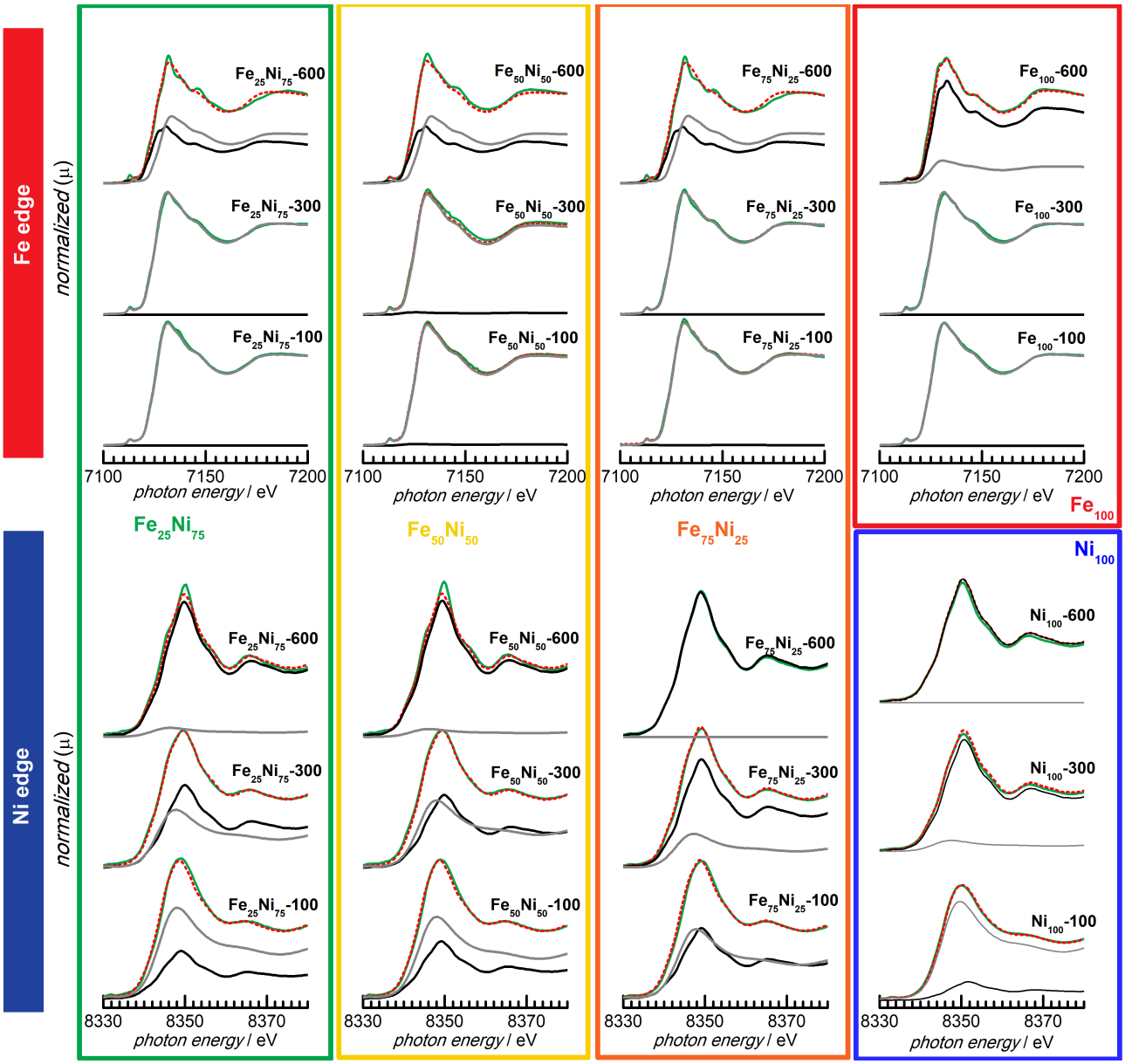

Figure S6: Linear combination fits (red dotted lines) using NiO (black lines) and $Ni(OH)_2$ (grey lines) for the Ni edge, and FeOOH (grey lines) and α-Fe_2O_3 (black lines) for the Fe edge are shown for select samples.

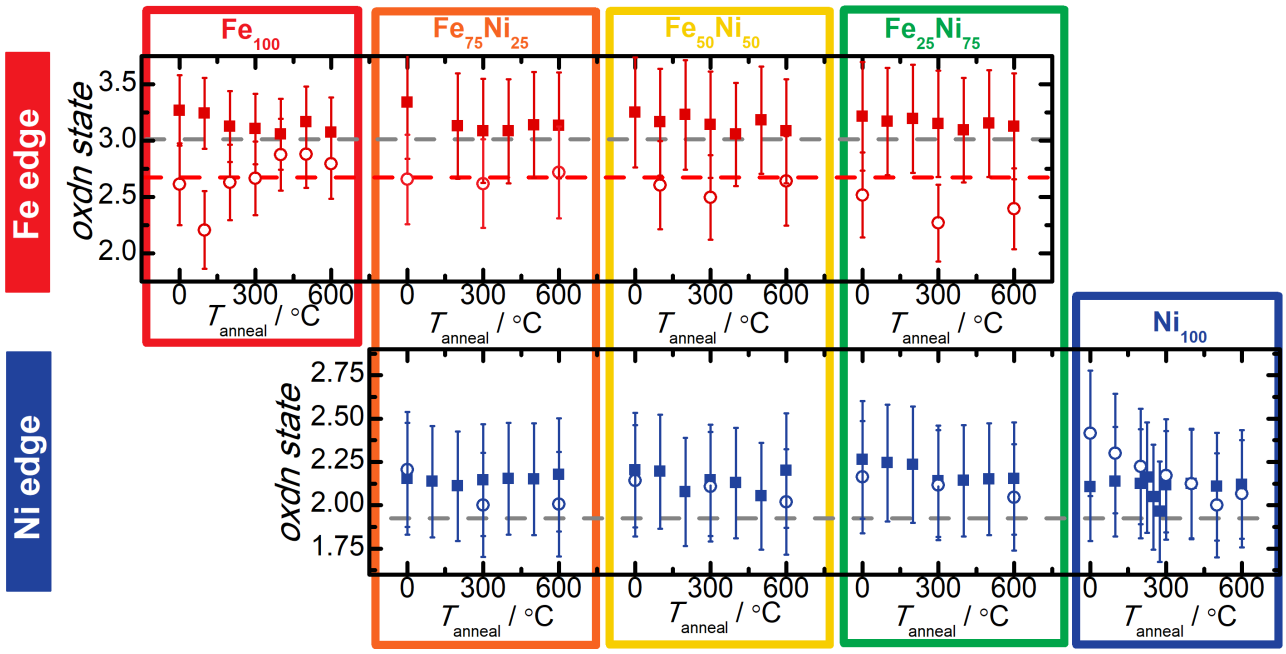

Figure S7: The oxidation states determined from XANES edge positions is plotted against T_{anneal} for Fe edges (upper row) and Ni edges (lower row). Oxidation states of **PO** samples are plotted as open symbols.

Electrochemistry

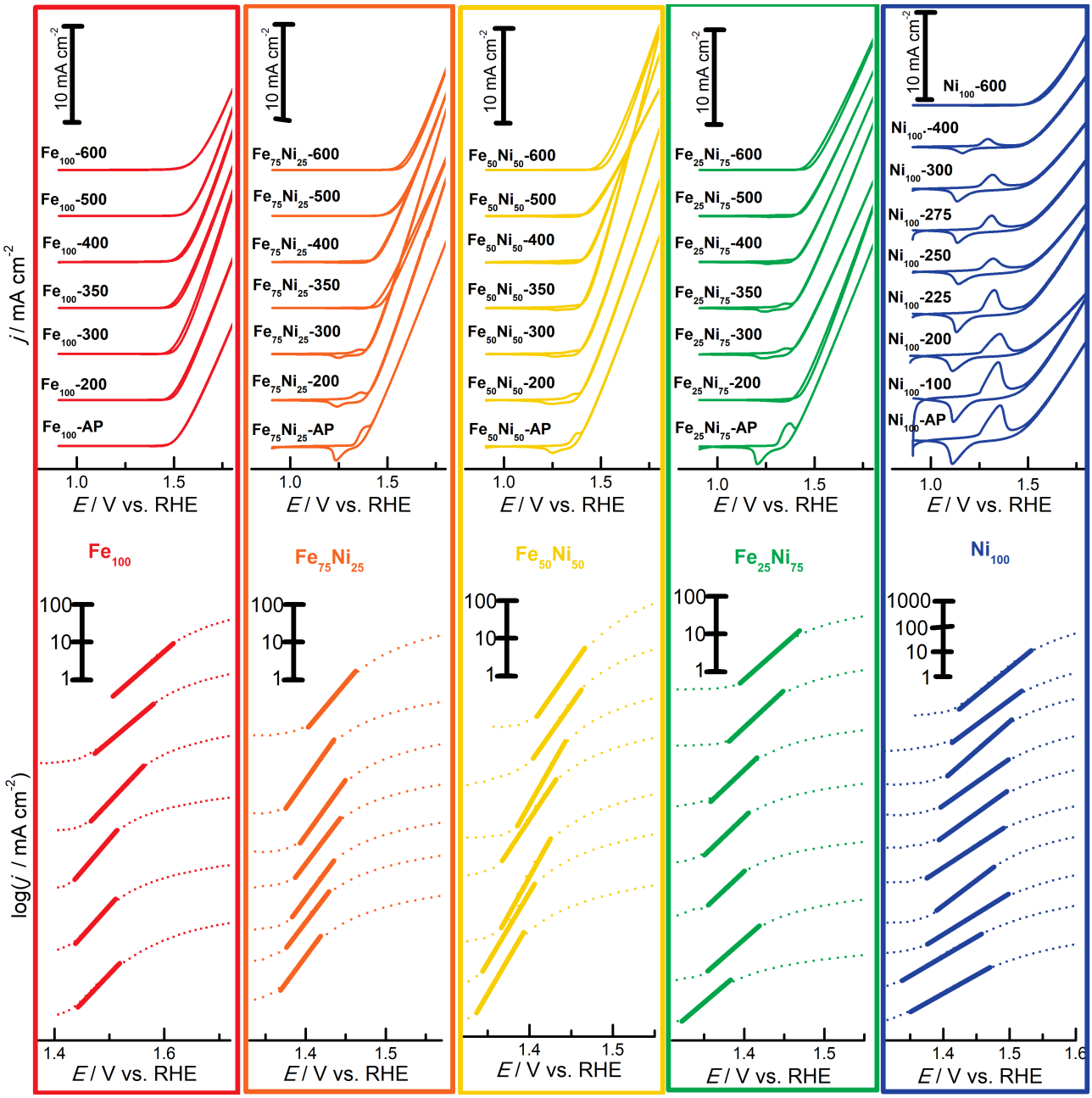

Figure S8: Current density plotted against applied potential (upper row) measured at a sweep rate of 0.01 Vs−1. Samples are denoted on each trace. Step-voltammetry is plotted in the lower row on a logarithmic vertical scale. The solid lines are linear fits to the data in the Tafel region. Data sets are offset for clarity.

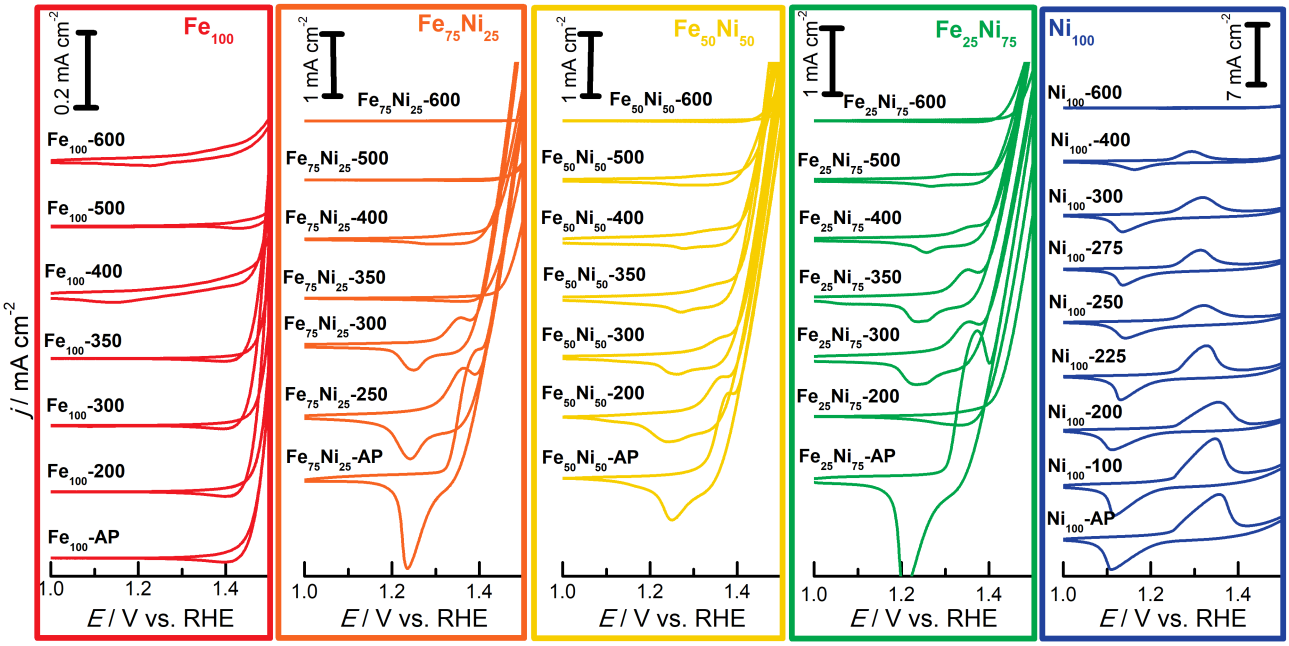

Figure S9: Current density plotted against applied potential vs. RHE, zoomed in to focus on the pre-catalytic region. Note the different scales in the plots.Data sets are offset for clarity.

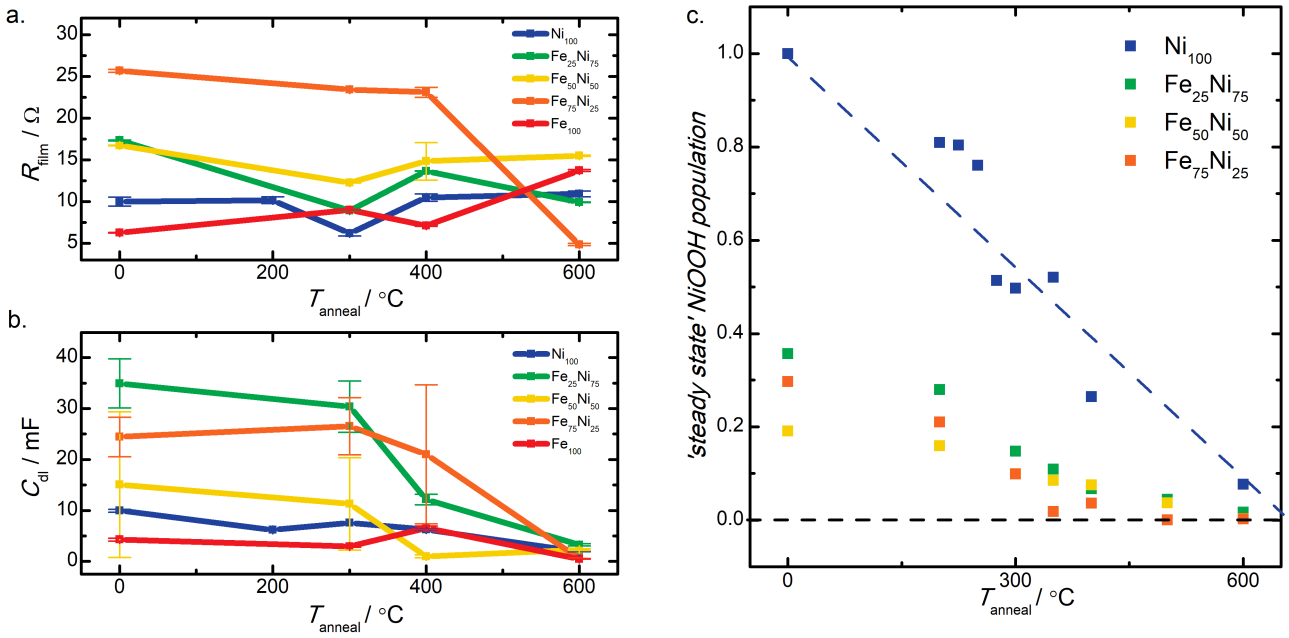

Figure S10: Film resistance R_{film} and double-layer capacitance C_{dl} determined from EIS are plotted in a. and b., respectively. c. shows the NiOOH population determined from integrating the pre-catalytic wave. Values are normalized to the **Ni$_{100}$-AP** value and the blue line is a guide to the eye fit to illustrate the behavior of the **Ni$_{100}$** series.

Electrochromism

The measured electrochromic response of samples annealed at 100 °C, 300 °C, and 600 °C to a 2.4 V potential step, applied at t = 0 s is plotted in Fig. S11, LHS panels. On the Fe-rich side (**Fe$_{100}$** through **Fe$_{50}$Fe$_{50}$**), the majority of coloring occurs slowly. For samples annealed at T_{anneal} = 300 °C and 600 °C this slow coloring is preceded by a small quick coloring step. For samples annealed at 100 °C the slow coloring occurs on a time scale of 25 s, which shortens with increased T_{anneal}. With higher Ni content the coloring occurs in two distinct steps of comparable magnitude; one fast step occurring in less than 1 s and a subsequent second slower step. The first step only leads to partial coloring of the sample, which decreases with T_{anneal}. The second slower step further colors the sample to approximately the same level in each sample series. When the potential is set to open current potential (OCP) samples in series **Fe$_{100}$** through **Fe$_{50}$Fe$_{50}$** bleach almost completely, while samples in series containing more Ni partially bleach to the coloring levels achieved in the first coloring step.

In addition to measuring coloration kinetics with applied potential step we utilize the electrochromic effect to track CVs. In the RHS panels of Fig. S11 we plot the electrochromic response to a single CV from 0.9 V to 2.4 V vs. RHE at 0.01 V s^{-1} sweep rate for samples annealed at 100 °C, 300 °C, and 600 °C. For the **Fe$_{100}$** series, the coloring occurs at catalytic onset and follows the applied potential continuously with a delay. Coloring occurs faster for higher T_{anneal}. Already small amounts of Ni incorporated into the system lead to a small coloring step before catalytic onset, which decreases in magnitude with $T_{\text{anneal}}$and increases in magnitude with increasing Ni content. After this initial coloring all samples colors further at lower coloring rates. This additional coloring does not coincide with the catalytic onset, which is signified by vertical dotted lines.

Fe and Ni oxides are well known to exhibit electrochromic behavior[54] and electrochromism in NiO_x has been well described.[55] In short, the reversible electrochromism with applied anodic potentials in NiO_x is attributed to the

$$\text{NiO or Ni(OH)}_2 \text{ (bleached)} \rightleftharpoons \text{NiOOH or NiOO (colored)}$$

reaction. Since these compounds are also OER intermediates, electrochromism enables us to directly monitor these intermediary concentrations.[25] FeO_x has received significantly less attention for their electrochromic properties, which is mostly due to low elecrochromic efficiency, slow dynamics, and partial irreversible coloring.[54] In aqueous solution the reversible electrochromic mechanism has been attributed to the

$$Fe(OH)_2 \text{ (bleached)} \rightleftharpoons FeOOH \text{ (colored)}$$

reaction.[56] For α-Fe_2O_3, an irreversible phase transition to Fe_3O_4 followed by hydration to $Fe(OH)_2$ preceeding the electrochromic reaction has been reported.[56] In our **Fe$_{100}$** sample series XANES fingerprinting initially shows FeOOH or α-Fe_2O_3 for low and high T_{anneal}, respectively, while all *post-operando* samples exhibit Fe_3O_4 signatures. Thus, it is likely that our samples follow the electrochromic mechanism described above and the coloring we observe is correlated to the FeOOH concentration.

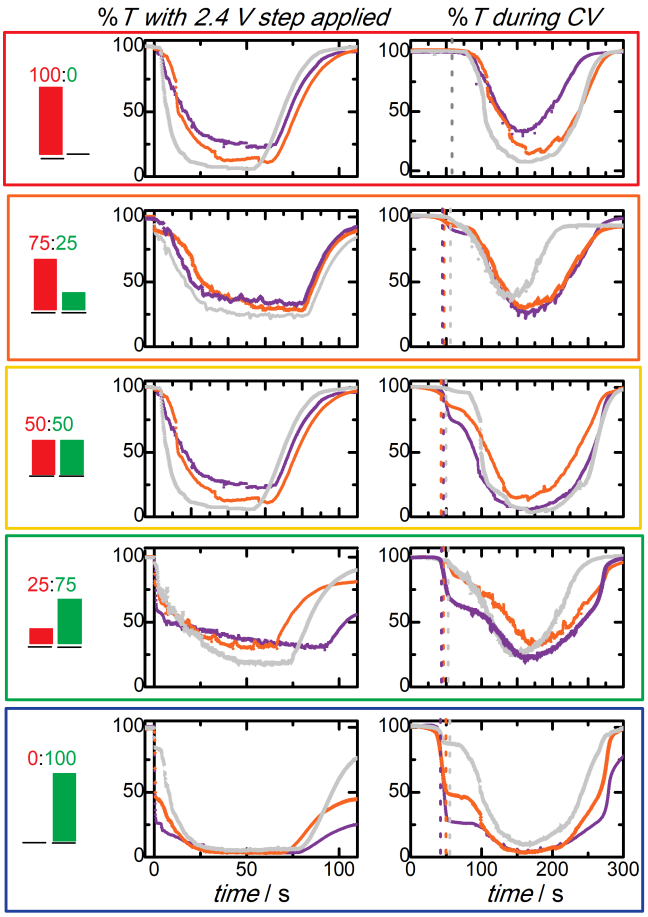

Figure S11: Electrochromic kinetics tracked over time; % Transmission at a wavelenght of 450 nm vs. time for a 2.4 V voltage step applied at t = 0 s (LHS column panels) and %T vs. time for tracking a single CV at 0.9 V to 2.4 V vs. RHE at a sweep rate of 0.01 Vs−1 (RHS column panels) for the sample compositions denoted on the LHS. In all panels samples annealed at 100 °C are plotted in purple, annealed at 300 °C in orange, and annealed at 600 °C in gray. The time of the catalytic onset is signified by vertical dotted lines in the respective colors.

Tables

Table S1: The EXAFS fit parameters coordination number N, energy offset E_0, first shell oxygen bond distances $R_{\mathrm{Ni-O}}$, second shell metal bond distances $R_{\mathrm{Ni-M}}$, oxygen Debye Waller factor σ^2(O), and metal Debye Waller factor σ^2(M) are listed for the Ni edges of the annealing series.

Sample	N	E_0 / eV	$R_{\mathrm{Ni-O}}$ / Å	$R_{\mathrm{Ni-M}}$ / Å	σ^2(O) / Å^{-2}	σ^2(M) / Å^{-2}
Ni_{100}-AP	4.5±0.4	-4.1±1.1	2.047±0.01	3.076±0.028	0.007±0.0015	0.033±0.0044
Ni_{100}-100	4.4±0.6	-3.9±1.5	2.047±0.009	3.057±0.018	0.007±0.0013	0.024±0.0023
Ni_{100}-200	4.8±0.8	-3.7±1.7	2.05±0.011	3.033±0.019	0.008±0.0017	0.024±0.0025
Ni_{100}-225	4.4±0.5	-3.3±1.2	2.055±0.012	3.026±0.018	0.007±0.002	0.021±0.0024
Ni_{100}-250	5.6±0.8	-2.5±1.3	2.072±0.017	2.982±0.011	0.01±0.0029	0.01±0.0015
Ni_{100}-275	5.8±0.9	-2±1.4	2.076±0.017	2.989±0.012	0.009±0.003	0.01±0.0016
Ni_{100}-300	5.6±0.5	-2.7±0.8	2.075±0.01	2.971±0.007	0.009±0.0017	0.009±0.0008
Ni_{100}-400	5.7±0.4	-2.7±0.7	2.076±0.01	2.962±0.006	0.008±0.0017	0.008±0.0007
Ni_{100}-500	6±0.4	-2.9±0.7	2.077±0.009	2.96±0.005	0.009±0.0015	0.008±0.0007
Ni_{100}-600	5.9±0.5	-2.8±0.8	2.077±0.012	2.958±0.007	0.008±0.0019	0.007±0.0008
$Fe_{25}Ni_{75}$-AP	4.7±0.5	-4±1.1	2.055±0.01	3.058±0.019	0.006±0.0016	0.024±0.0028
$Fe_{25}Ni_{75}$-100	4.4±0.8	-1.6±0	2.061±0.023	3.076±0.023	0.007±0.0018	0.022±0.0029
$Fe_{25}Ni_{75}$-200	4.7±0.7	-3.7±1.5	2.051±0.009	3.017±0.014	0.008±0.0014	0.02±0.0018
$Fe_{25}Ni_{75}$-300	4.7±0.6	-2.4±1.1	2.063±0.013	3.007±0.016	0.008±0.0021	0.019±0.0021
$Fe_{25}Ni_{75}$-400	5.1±0.6	-2.1±1.2	2.054±0.013	2.974±0.014	0.007±0.002	0.015±0.0018
$Fe_{25}Ni_{75}$-500	5.5±0.9	-1.2±1.7	2.062±0.019	2.973±0.017	0.007±0.003	0.012±0.0021
$Fe_{25}Ni_{75}$-600	6±1.1	-0.7±1.7	2.068±0.022	2.976±0.018	0.009±0.0036	0.012±0.0023
$Fe_{50}Ni_{50}$-AP	4.7±1.2	-1.8±2.7	2.067±0.017	3.084±0.028	0.007±0.0025	0.021±0.0036
$Fe_{50}Ni_{50}$-100	4.4±0.4	-3.1±0.8	2.06±0.008	3.043±0.012	0.006±0.0013	0.02±0.0017
$Fe_{50}Ni_{50}$-200	4.6±0.4	-2.8±0.8	2.063±0.009	3.025±0.012	0.007±0.0014	0.02±0.0017
$Fe_{50}Ni_{50}$-300	4.7±0.3	-3±0.7	2.062±0.007	3.013±0.009	0.008±0.0012	0.019±0.0012
$Fe_{50}Ni_{50}$-400	5.1±0.4	-2.6±0.7	2.066±0.008	2.994±0.008	0.009±0.0013	0.017±0.0011
$Fe_{50}Ni_{50}$-500	5.3±0.5	-2.7±0.8	2.063±0.01	2.986±0.009	0.009±0.0016	0.015±0.0012
$Fe_{50}Ni_{50}$-600	5.6±0.9	-1.5±1.6	2.06±0.019	2.967±0.017	0.007±0.003	0.012±0.0021
$Fe_{75}Ni_{25}$-AP	4±0.8	-5.3±2.5	2.037±0.013	3.075±0.022	0.005±0.0018	0.016±0.0024
$Fe_{75}Ni_{25}$-100	4.4±0.4	-3.6±0.8	2.062±0.008	3.04±0.01	0.007±0.0014	0.018±0.0014
$Fe_{75}Ni_{25}$-200	4.9±0.5	-3.5±0.8	2.065±0.01	3.013±0.01	0.009±0.0017	0.015±0.0013
$Fe_{75}Ni_{25}$-300	5.2±0.4	-3.1±0.7	2.07±0.008	2.998±0.007	0.009±0.0015	0.014±0.001
$Fe_{75}Ni_{25}$-400	5.7±0.5	-2.6±0.8	2.076±0.011	2.981±0.008	0.009±0.0018	0.011±0.001
$Fe_{75}Ni_{25}$-500	5.7±0.6	-3.4±0.9	2.075±0.012	2.971±0.008	0.009±0.002	0.01±0.001
$Fe_{75}Ni_{25}$-600	5.8±0.5	-2.5±0.8	2.075±0.011	2.966±0.007	0.008±0.0018	0.009±0.0009

Table S2: The EXAFS fit parameters coordination number N, energy offset E_0, first shell oxygen bond distances $R_{\mathrm{Fe-O}}$, second shell metal bond distances $R_{\mathrm{Fe-M}}$, oxygen Debye Waller factor σ^2(O), and metal Debye Waller factor σ^2(M) are listed for the Fe edges of the annealing series.

Sample	N	E_0 / eV	$R_{\mathrm{Fe-O}}$ / Å	$R_{\mathrm{Fe-M}}$ / Å	σ^2(O) / Å^{-2}	σ^2(M) / Å^{-2}
Fe_{100}-AP-PO	6.7±1	6.4±1.7	1.975±0.011	3.136±0.003	0.011±0.0017	0.022±0.003
Fe_{100}-100-PO	6.4±0.7	5.8±1.3	1.959±0.008	3.114±0.002	0.01±0.0013	0.021±0.002
Fe_{100}-200-PO	5.9±0.7	4.8±1.3	1.945±0.008	3.095±0.002	0.009±0.0012	0.022±0.0022
Fe_{100}-300-PO	5.7±0.7	5.1±1.5	1.942±0.009	3.088±0.002	0.009±0.0014	0.02±0.0023
Fe_{100}-400-PO	6.9±1.1	2.4±1.7	1.958±0.018	2.988±0.002	0.01±0.003	0.01±0.0021
Fe_{100}-500-PO	6.9±1.2	2.4±1.7	1.96±0.018	2.986±0.002	0.01±0.0032	0.009±0.0022
Fe_{100}-600-PO	7±1.2	2.4±1.7	1.961±0.019	2.984±0.002	0.01±0.0032	0.009±0.0021
$Fe_{25}Ni_{75}$-AP	6.1±1.1	1.1±2.1	1.953±0.013	3.1±0.003	0.01±0.002	0.02±0.003
$Fe_{25}Ni_{75}$-100	6.2±1	2.2±1.8	1.971±0.011	3.123±0.003	0.01±0.0017	0.021±0.0027
$Fe_{25}Ni_{75}$-200	5.8±1	0.8±2	1.947±0.012	3.082±0.003	0.01±0.0019	0.019±0.0027
$Fe_{25}Ni_{75}$-300	5.6±0.8	2.3±1.7	1.95±0.01	3.088±0.002	0.009±0.0016	0.018±0.0023
$Fe_{25}Ni_{75}$-400	6.9±1.2	0.8±1.9	1.941±0.012	3.061±0.002	0.011±0.0021	0.016±0.0022
$Fe_{25}Ni_{75}$-500	6.9±1.2	3.1±1.7	1.949±0.018	3.071±0.003	0.011±0.0033	0.012±0.0026
$Fe_{25}Ni_{75}$-600	7.3±1.3	2.9±1.8	1.945±0.019	3.066±0.003	0.012±0.0036	0.012±0.0026
$Fe_{50}Ni_{50}$-AP	6.4±1.3	3±2.3	1.976±0.014	3.134±0.004	0.01±0.0022	0.02±0.0036
$Fe_{50}Ni_{50}$-100	5.4±0.8	2.6±1.6	1.962±0.01	3.11±0.002	0.009±0.0014	0.017±0.0021
$Fe_{50}Ni_{50}$-200	5.7±0.9	1.2±1.8	1.951±0.011	3.088±0.002	0.01±0.0017	0.018±0.0024
$Fe_{50}Ni_{50}$-300	5.7±1.1	1.8±2.1	1.952±0.013	3.086±0.003	0.009±0.0019	0.017±0.0026
$Fe_{50}Ni_{50}$-400	5.5±0.9	1.1±1.8	1.945±0.011	3.074±0.002	0.009±0.0017	0.016±0.0021
$Fe_{50}Ni_{50}$-500	6.1±1.3	2.6±2.3	1.972±0.014	3.117±0.003	0.009±0.0022	0.016±0.0027
$Fe_{50}Ni_{50}$-600	6±1	0.1±1.8	1.958±0.011	3.069±0.002	0.009±0.0018	0.014±0.002
$Fe_{75}Ni_{25}$-AP	6.4±0.9	2.1±1.5	1.984±0.013	3.176±0.025	0.007±0.0022	0.018±0.0036
$Fe_{75}Ni_{25}$-100	6.8±1.3	1.8±1.3	1.964±0.012	3.131±0.02	0.008±0.002	0.017±0.0028
$Fe_{75}Ni_{25}$-200	5.9±0.9	-0.1±1.6	1.95±0.015	3.081±0.021	0.009±0.0026	0.015±0.0028
$Fe_{75}Ni_{25}$-300	5.9±0.9	-0.9±1.6	1.936±0.015	3.062±0.021	0.01±0.0026	0.015±0.0028
$Fe_{75}Ni_{25}$-400	5.8±0.9	-1.5±1.6	1.927±0.014	3.047±0.021	0.01±0.0025	0.015±0.0028
$Fe_{75}Ni_{25}$-500	5.7±0.9	-0.5±1.7	1.933±0.015	3.058±0.024	0.01±0.0026	0.017±0.0031
$Fe_{75}Ni_{25}$-600	7.1±0.9	1.9±1.2	1.942±0.014	3.053±0.015	0.013±0.0027	0.011±0.0019

Table S3: The EXAFS fit parameters coordination number N, energy offset E_0, first shell oxygen bond distances $R_{\mathrm{Ni-O}}$, second shell metal bond distances $R_{\mathrm{Ni-M}}$, oxygen Debye Waller factor σ^2(O), and metal Debye Waller factor σ^2(M) are listed for the Ni edges of the *post-operando* series.

Sample	N	E_0 / eV	$R_{\mathrm{Ni-O}}$ / Å	$R_{\mathrm{Ni-M}}$ / Å	σ^2(O) / Å^{-2}	σ^2(M) / Å^{-2}
Ni_{100}-AP-PO	4.3±0.8	-4.2±2.1	1.975±0.022	2.927±0.033	0.013±0.0039	0.027±0.0044
Ni_{100}-100-PO	4.2±0.6	-3.7±1.5	2.005±0.015	2.959±0.024	0.012±0.0026	0.028±0.0032
Ni_{100}-200-PO	4.1±0.3	-3±0.8	2.024±0.008	2.973±0.009	0.01±0.0015	0.018±0.0013
Ni_{100}-300-PO	4.7±0.3	-2.8±0.7	2.036±0.009	2.953±0.006	0.012±0.0016	0.011±0.0008
Ni_{100}-400-PO	5.1±0.4	-2.4±0.7	2.058±0.01	2.955±0.006	0.01±0.0018	0.009±0.0008
Ni_{100}-500-PO	5.6±0.4	-2.8±0.8	2.071±0.01	2.956±0.006	0.008±0.0016	0.008±0.0007
Ni_{100}-600-PO	5.4±0.4	-2.7±0.8	2.068±0.01	2.957±0.006	0.008±0.0016	0.008±0.0008
$Fe_{25}Ni_{75}$-100-PO	4.5±0.4	-3.4±0.8	2.052±0.008	3.038±0.011	0.007±0.0014	0.019±0.0016
$Fe_{25}Ni_{75}$-300-PO	3.7±0.6	-2.2±1.4	2.063±0.017	2.956±0.012	0.008±0.0026	0.01±0.0015
$Fe_{25}Ni_{75}$-600-PO	5.7±0.5	-2.9±0.8	2.072±0.011	2.96±0.007	0.008±0.0018	0.008±0.0009
$Fe_{50}Ni_{50}$-100-PO	4.5±0.6	-3.4±1.5	2.051±0.009	3.047±0.014	0.007±0.0014	0.019±0.0017
$Fe_{50}Ni_{50}$-300-PO	4.8±0.3	-3.6±0.6	2.053±0.006	2.991±0.007	0.009±0.0011	0.017±0.0009
$Fe_{50}Ni_{50}$-600-PO	5.5±0.5	-2.3±0.8	2.066±0.01	2.966±0.008	0.008±0.0016	0.011±0.001
$Fe_{75}Ni_{25}$-100-PO	4.7±0.3	-4.1±0.6	2.052±0.006	3.031±0.01	0.007±0.001	0.024±0.0015
$Fe_{75}Ni_{25}$-300-PO	4.6±0.3	-2.6±0.6	2.054±0.007	2.999±0.009	0.008±0.0011	0.019±0.0011
$Fe_{75}Ni_{25}$-600-PO	5.6±0.9	-1.7±1.5	2.061±0.018	2.964±0.015	0.007±0.0028	0.012±0.0019

Table S4: The EXAFS fit parameters coordination number N, energy offset E_0, first shell oxygen bond distances $R_{\mathrm{Fe-O}}$, second shell metal bond distances $R_{\mathrm{Fe-M}}$, oxygen Debye Waller factor σ^2(O), and metal Debye Waller factor σ^2(M) are listed for the Fe edges of the *post-operando* series.

Sample	N	E_0 / eV	$R_{\mathrm{Ni-O}}$ / Å	$R_{\mathrm{Fe-M}}$ / Å	σ^2(O) / Å^{-2}	σ^2(M) / Å^{-2}
Fe_{100}-AP-PO	5.7±0.8	6.1±1.6	1.959±0.01	3.119±0.004	0.01±0.0015	0.028±0.004
Fe_{100}-100-PO	4.4±1.1	6.5±3.1	1.958±0.019	3.085±0.007	0.009±0.0027	0.027±0.0074
Fe_{100}-200-PO	5.5±0.6	5±1.3	1.948±0.008	3.106±0.003	0.01±0.0012	0.027±0.003
Fe_{100}-300-PO	5.2±0.8	3.8±1.9	1.935±0.011	3.061±0.003	0.009±0.0016	0.023±0.0034
Fe_{100}-400-PO	5.8±1.1	2.4±2	1.949±0.02	2.992±0.003	0.009±0.0034	0.012±0.0029
Fe_{100}-500-PO	5.6±1	2.2±1.9	1.946±0.019	2.99±0.003	0.008±0.0032	0.011±0.0027
Fe_{100}-600-PO	5.7±1	2.4±1.8	1.948±0.018	2.99±0.003	0.009±0.003	0.011±0.0026
$Fe_{25}Ni_{75}$-100-PO	5.3±0.8	6.6±1.9	1.971±0.012	3.134±0.005	0.01±0.0017	0.027±0.0046
$Fe_{25}Ni_{75}$-300-PO	5.1±1	4±2.4	1.945±0.015	3.063±0.004	0.01±0.0022	0.022±0.0038
$Fe_{25}Ni_{75}$-600-PO	5±0.7	5.2±1.6	1.944±0.011	3.06±0.002	0.01±0.0016	0.017±0.0021
$Fe_{50}Ni_{50}$-100-PO	5.8±1	6.2±2	1.968±0.013	3.121±0.004	0.01±0.0019	0.023±0.0036
$Fe_{50}Ni_{50}$-300-PO	4.9±0.8	4.2±2	1.942±0.012	3.073±0.003	0.009±0.0018	0.021±0.0032
$Fe_{50}Ni_{50}$-600-PO	5.2±0.5	5.4±1	1.933±0.009	3.046±0.002	0.008±0.0016	0.013±0.0016
$Fe_{75}Ni_{25}$-100-PO	5.6±0.9	5.7±1.9	1.962±0.012	3.116±0.004	0.01±0.0018	0.025±0.004
$Fe_{75}Ni_{25}$-300-PO	5.4±0.9	5.2±2	1.945±0.013	3.082±0.004	0.01±0.0019	0.023±0.0037
$Fe_{75}Ni_{25}$-600-PO	5.8±0.6	5.8±1.1	1.938±0.011	3.053±0.002	0.01±0.0019	0.013±0.0018

Table S5: Table of EIS fit parameters for all Fe containing compounds. Charge transfer resistance R_{ct}, film resistance R_{film}, film capacitance C_{film}, and series resistance R_s

Sample	R_{ct} / Ω	C_{dl} / mF	R_{film} / Ω	C_{film} / μF	R_s / Ω
Fe_{100}-600	17.4 ± 0.11	0.4 ± 0.02	13.7 ± 0.12	0.003 ± 0.0002	7.1 ± 0.08
Fe_{100}-400	7.8 ± 0.15	6.6 ± 0.3	7.1 ± 0.09	0.0116 ± 0.0009	7.0 ± 0.04
Fe_{100}-300	4.4 ± 0.05	2.9 ± 0.2	9 ± 0.03	0.0385 ± 0.0014	7.4 ± 0.02
Fe_{100}-AP	2.9 ± 0.04	4.3 ± 0.3	6.3 ± 0.04	0.0198 ± 0.0012	7.5 ± 0.03
$Fe_{75}Ni_{25}$-600	9.4 ± 0.18	0.6 ± 0.02	4.9 ± 0.13	0.0093 ± 0.0017	8.1 ± 0.06
$Fe_{75}Ni_{25}$-400	21.3 ± 11.58	2.1 ± 1.3	23.1 ± 0.59	0.0053 ± 0.0006	6.4 ± 0.28
$Fe_{75}Ni_{25}$-300	4.8 ± 0.57	2.7 ± 0.5	23.4 ± 0.08	0.0585 ± 0.0022	6.7 ± 0.04
$Fe_{75}Ni_{25}$-AP	3.4 ± 0.24	2.4 ± 0.4	25.7 ± 0.18	0.0511 ± 0.004	7.8 ± 0.08
$Fe_{50}Ni_{50}$-600	4.3 ± 0.08	2.3 ± 0.2	15.5 ± 0.07	0.0029 ± 0.0001	7.2 ± 0.06
$Fe_{50}Ni_{50}$-400	40.2 ± 2.47	1.0 ± 0.3	14.8 ± 2.25	0.0015 ± 0.001	4.4 ± 0.07
$Fe_{50}Ni_{50}$-300	0.8 ± 0.17	1.1 ± 0.09	12.3 ± 0.04	0.0923 ± 0.014	5.1 ± 0.25
$Fe_{50}Ni_{50}$-AP	1 ± 0.27	1.5 ± 0.1	16.7 ± 0.06	0.0581 ± 0.0103	6.2 ± 0.05
$Fe_{25}Ni_{75}$-600	2.3 ± 0.03	3.3 ± 0.2	9.9 ± 0.05	0.0067 ± 0.0003	7.2 ± 0.05
$Fe_{25}Ni_{75}$-400	1.6 ± 0.04	1.2 ± 0.1	13.7 ± 0.03	0.0037 ± 0.0001	7.4 ± 0.03
$Fe_{25}Ni_{75}$-300	1.4 ± 0.08	3.0 ± 0.5	8.9 ± 0.05	0.0062 ± 0.0003	4.9 ± 0.04
$Fe_{25}Ni_{75}$-AP	1.8 ± 0.1	3.5 ± 0.5	17.3 ± 0.06	0.002 ± 0.0001	7.6 ± 0.05